Università degli Studi di Ferrara
DOTTORATO DI RICERCA IN
SCIENZE DELL'INGEGNERIA

CICLO XXVII

COORDINATORE Prof. Trillo Stefano

A NOVEL PTF-BASED EXPERIMENTAL CHARACTERISATION FOR PORO-ELASTIC LINERS: METHOD AND SAMPLING CRITERION

Settore Scientifico Disciplinare ING/IND 11

Dottorando
Dott. Veronesi Giorgio

Tutore
Prof. Prodi Nicola

Cotutori
Ing. Nijman Eugenius J. M.

Dott. Rejlek Jan

Anni 2012/2014

This research work has been carried out at the Virtual Vehicle Research Center and it has been funded by the European Commission within the Marie Curie Action project GRESIMO. I would like to express my deepest gratitude to my mentors Eugène Nijman and Jan Rejlek. Finally, I would like to address my acknowledgement to Prof. Nicola Prodi for supporting my PhD work at the University of Ferrara.

Giorgio Veronesi
Graz, March 2015

Contacts

Giorgio Veronesi

Virtual Vehicle Research Center
Inffeldgasse 21A
8010, Graz, Austria
+43 (0)316 8739810
giorgio.veronesi@v2c2.at

via San Martino Carano 55
41037, Mirandola, Italy
+39 338 1877878
giorgio.veronesi@gmail.com

Ai miei genitori Giuseppina e Arturo.

Abstract

The vibro-acoustic behaviour of structures coupled with poroelastic trims and fluid cavities can be predicted by means of the Patch Transfer Function (PTF) approach. The PTF is a sub-structuring procedure that allows to couple different sub-systems via impedance relations determined at their common interfaces. The coupling surfaces are discretised into elementary areas called patches. Since the patch impedances can be determined in either computational or experimental manner, the PTF approach offers high degrees of modularity. For sub-systems, which allow for an efficient numerical characterisation, simulation schemes should be adopted, whereas for sub-systems, which involve highly complex models, measurements might offer a cost-efficient alternative. In the first part of the work the PTF approach is presented.

Next, the sampling criterion for the PTF description of the vibratory field and sound radiation from structures is discussed. When studying the sound radiating from vibrating structures the surface is discretised into elemental areas also referred to as patches. Here the special case of a simply supported baffled plate excited by a broadband point force is considered. It is shown that accurate approximation of the radiated power may be obtained well beyond the frequency limit imposed by the structural Nyquist sampling criterion, provided the complex-valued vibration field is averaged over each patch. This is due to the fact that the averaging process not only reduces the structural velocity but simultaneously determines an increased radiation efficiency. An analytical expression is provided allowing the optimisation of the patch size given a desired accuracy level for the assessment of the radiated power.

In the third part of the work a novel PTF-based experimental method for the characterisation of poroelastic materials is proposed. The novelty of the methodology proposed consists in the fact that the trim characterisation no longer relies on a material micro-model (i.e. Biot), whose parameters are often difficult to be acquired. The specimen is considered as a single component, therefore no separation of layers is necessary. An air layer correction for surface impedance measurement is discussed.

Finally, the PTF approach proposed has been applied on a laboratory test case, consisting of a trimmed plate coupled to a rigid acoustic cavity. The PTF reconstruction has been successfully validated through a measurement conducted on the fully assembled system.

Riassunto

Nel presente lavoro il comportamento di sistemi vibro-acustici accoppiati è analizzato tramite il metodo noto in letteratura come Patch Transfer Function (PTF). La PTF è una metodologia di accoppiamento che permette di accoppiare sotto-domini una volta note le matrici di impedenza determinate alle rispettive interfacce. Le superfici di accoppiamento sono discretizzate in superfici elementari dette patch. Siccome le relazioni di impedenza tra le patch possono essere determinate per via sperimentale, numerica e talvolta per via analitica, la PTF offre piena flessibilità sulla scelta della tecnica di caratterizzazione del singolo sottosistema. Nel caso di sottosistemi caratterizzati da una complessità relativamente semplice un calcolo numerico può essere preferito, in caso di sottosistemi particolarmente complessi indagini sperimentali possono rappresentare una alternativa più efficiente.

La scelta della raffinatezza della suddivisione delle interfacce tra i sotto-sistemi determina la massima frequenza raggiungibile dal metodo di calcolo. Una stima accurata della potenza sonora irradiata può essere ottenuta ben oltre il limite imposto dal criterio di campionamento di Nyquist, applicato alla lunghezza d'onda strutturale, a patto di assegnare alle patch una velocità determinata tramite una media complessa del campo di vibrazione della struttura. La media operata sul campo complesso di velocità determina una riduzione della velocità strutturale e simultaneamente un incremento dell'efficienza di radiazione. Nel presente lavoro è derivato un modello analitico per l'ottimizzazione della discretizzazione in base alla scelta del livello di accuratezza nella stima della potenza acustica irradiata.

Nel presente lavoro è presentata una nuova metodologia per la caratterizzazione sperimentale di materiali poro-elastici, completamente compatibile con la PTF. Il principale vantaggio della metodologia proposta risiede nel fatto che il materiale è considerato come un unico sistema. Pertanto, in caso di materiali multistrato, non risulta necessario separare i singoli strati per determinarne le proprietà meccaniche e i parametri di Biot. Inoltre nel presente lavoro è presentata una metodologia per eliminare l'influenza della distanza campione-sensore nelle misure di impedenza superficiale effettuate tramite sonde PU.

Infine, la PTF è stata applicata a un sistema costituito da una piastra metallica, eventualmente smorzata da un pannelo di materiale poro-elastico, accoppiata a una cavità rigida. La ricostruzione del livello di pressione sonora (SPL) all'interno della cavità acustica per mezzo della PTF è stata confrontata con una misura diretta eseguita sul sistema accoppiato.

Contents

Nomenclature

A_1, A_2, B	constants defined by Eq. (2.55)
a, b	panel dimensions $[m]$
C^2	patch velocity constant
c_0	speed of sound in air $[m/s]$
c_1, c_2	constants defined by Eq. (2.55)
D	plate bending stiffness $[Nm]$
d	patch dimension $[m]$
E	Young modulus $[Pa]$
F	force $[N]$
f	frequency $[Hz]$
f_c	plate coincidence frequency $[Hz]$
f_{cp}	patch-plate coincidence frequency $[Hz]$ $f_{cp} = f_{N,0}$
$f_{N,0}$	acoustic Nyquist frequency $[Hz]$ $f_{N,0} = f_{cp}$
$f_{N,s}$	structural Nyquist frequency $[Hz]$
j	imaginary unit
k_0	acoustic wavenumber $[1/m]$
k_b	plate bending wavenumber $[1/m]$
k_p	patch-plate wavenumber $[1/m]$
k_r	spatial transform wavenumber $[1/m]$
k_s	structural wavenumber $[1/m]$
k_x	x-projection of k_s $[1/m]$
k_y	y-projection of k_s $[1/m]$
ln	natural logarithm
m, n	mode counters
$\overline{m}$	mass per unit area $[kg/m^2]$
$\frac{\Delta N}{\Delta \omega}$	modal density $[s]$
N_p	number of patches

N_{px}, N_{py}	no. of patches in x-, y-direction
p	sound pressure
q, r	patch-plate parametric coordinates
$\boldsymbol{r}$	position vector $[m]$
S	plate surface $[m^2]$
SPL	sound pressure level $[dB]$, p_{ref}=20$\cdot 10^{-6}$ $[Pa]$
t	plate thickness $[m]$
t	time $[s]$
v	structural velocity $[m/s]$
$\hat{v}_{m,n}$	modal velocity amplitude $[m/s]$
W	sound power $[W]$
w_z	out-of-plane displacement field $[m]$
x, y	cartesian coordinate
x_0, y_0	force position $[m]$
Y, y	mobility $[m/sPa]$
Z, z	impedance $[sPa/m]$
α	wave direction $[rad]$
β	defined in Eq. (2.51) $[s^{-1/2}]$
Γ_a	acoustic boundary
Γ_{pa}	porous-acoustic boundary
Γ_{sa}	structural-acoustic boundary
Γ_{sp}	structural-porous boundary
γ	d/c_0 $[s]$
δ	Dirac function in Chapter 1
δ	$k_p d = 2\pi/2.3$ in Chapter 2
∇^2	Laplacian operator
ε	power error $[W]$
ϵ	power error $[dB]$
η	damping loss factor
$\Lambda_{m,n}$	norm $[kg]$
λ_p	patch-plate wavelength $[m]$
λ_s	structural wavelength $[m]$
μ	normalised wavenumber
ρ	mass density $[kg/m^3]$
ρ_0	air density $[kg/m^3]$
σ	radiation efficiency

φ	phase $[Deg]$
$\phi_i(\boldsymbol{r})$	acoustic mode shapes
$\varphi_{m,n}(x,y)$	structural mode shapes
Ω_a	acoustic domain
Ω_p	porous domain
Ω_s	structural domain
ω	angular frequency $[rad/s]$
$\omega_{m,n}$	plate natural frequencies $[rad/s]$
$\omega_{mc,nc}$	plate centre band frequency $[rad/s]$

List of Figures

List of Tables

Chapter 1

Coupled vibro-acoustic problems

1.1 Introduction

Nowdays transportation industry is driven by the need to offer fuel efficient and eco-friendly mobility. Concerning the aerospace transportation of goods and passengers the European Union (EU) has set a target regarding CO_2 emissions for all the flights arriving and departing in EU countries. In the automotive market customers are asking for efficient vehicles and legislators are reducing carbon dioxide limits in order to reach the targets set by international agreements. In 1998, the European Automobile Manufacturers' Association (ACEA) adopted a commitment to reduce average emissions from new cars sold to 140 grams of CO_2 per kilometre by 2008. The European Community's regulation No 443/2009 sets the current emissions limits for passenger cars. Currently, there is an undergoing amendment in order to implement new severe targets for the upcoming years. If the new limits will be introduced in the EU light duty vehicles market, car manufacturers will be obliged to meet the target of 130 g of CO_2 per kilometre for the averaged fleet emission by 2015 and an average of 95 g/km by 2020. Such reduction of fuel consumption and carbon dioxide pollution is mainly pursued by means of lightweight design, downsizing of internal combustion engines and hybrid powertrains.

Unfortunately, the lightweight design is expected to deteriorate the air borne insulation performance of transportation vehicles. Therefore a new challenge is arising, namely the conflict between NVH and lightweight targets has to be solved in order to satisfy the targets set in the product definition phase. Lightweight structures show strong interaction with sound packages, thus an efficient tool for the accurate description of structure-liner-cavity interaction in the frequency range between 20-1000 Hz is necessary in order to optimise the acoustic design of the future vehicles. The state-of-the-art for the analysis of coupled vibro-acoustic problems involving porous materials is represented by the Biot-based fully coupled FE modelling. In general, these calculations are very time consuming and are limited to the low frequency range. Moreover, a very detailed knowledge of the Biot-parameters of the layered trim materials is required as an input for the calculation scheme, which are however often not available. In order to overcome these disadvantages an alternative characterisation procedure for typical

sound packages materials is demanded. In particular, this work is focused on the development of a novel and efficient experimental trim characterisation method and its implementation in a coupling procedure. The aim of this work is to provide an effective and reliable tool to analyse vibro-acoustic problems in the low and mid-frequency range where strong interaction between structure, liner and cavity typically appears.

In this work the Patch Transfer Function (PTF) approach is used to solve the coupled structural-porous-acoustic problem. The PTF Method has been developed by Ouisse et al. [1] and it has been applied to several acoustic problems later on. Pavic [2] used the PTF technique for source characterisation, Maxit et al. [3] improved the approach for structures coupled to heavy fluid. Moreover, Guyader et al. [4] and Chazot et al. [5] solved a transmission loss problem. Aucejo et al. [6] studied the convergence of the methodology when applied to heavy fluids. Later, Rejlek et al. [7] implemented the PTF method for coupled vibro-acoustic problems. Veronesi et al. [8] and Albert et al. [9] applied the PTF approach to coupled vibro-acoustic problems involving porous materials.

The main advantage of the methodology proposed is that each physical sub-system can be characterised in either experimental or numerical manner. The possibility to pursue an experimental characterisation of sub-system interfaces allows for a reduction of the computational time. Moreover the methodology is fully modular therefore the effect of different liners on the full-system can be predicted.

1.2 Problem statement

Let us consider a three-dimensional fully coupled vibro-acoustic problem, see Fig. 1.1. The structural part Ω_s consists of a thin flat plate subjected to (i) boundary conditions imposed at the physical boundary Γ_{sa}, Γ_{sp}, (ii) a harmonic point force $Fe^{j\omega t}$ acting in the out-of-plane direction at the position r'_F and (iii) the acoustic pressure loading p arising from the coupling to an acoustic domain along the structural-acoustic interface Γ_{sa}, or to the pressure loading and velocity arising from the coupling to a porous domain at the interface Γ_{sp}.

1.2.1 Structural part

The structural problem consists of a plate Ω_s characterised by its density ρ_s, elasticity modulus E, material loss factor η, the Poisson's ratio ν and the thickness t. The plate is subjected to a point force F acting at position directed in the out-of-plane direction. The structural displacement field $w_z(\mathbf{r}')$ is governed by the steady-state dynamic equation

$$\nabla^4 w_z(\mathbf{r}') - k_b^4 w_z(\mathbf{r}') = \frac{p}{D} + \frac{F}{D}\delta(\mathbf{r}'_F), \tag{1.1}$$

based on Kirchhoff's thin plate theory for the out-of-plane bending motion. In Eq. (1.1), ∇^2 is the Laplacian operator, δ is the Dirac delta function, k_b is the bending wave number and D is the bending stiffness. At the physical boundary a non-overlapping set

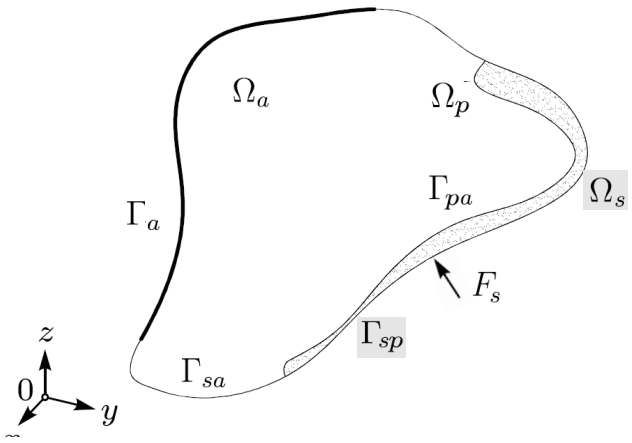

Figure 1.1: A fully coupled vibro-acoustic problem.

of boundary conditions is prescribed. In order for the problem to be well-posed, two boundary conditions need to be defined at each point of the boundary simultaneously [10]. In the structural problem, the structural-acoustic coupling effects are incorporated as a distributed transverse force by extending the particular solution function of the governing differential equation. A more detailed analytical description of the structural problem can be found in [10].

1.2.2 Poroelastic part

The porous part Ω_p consists of an isotropic porous material applied on a partition of the structural domain at the interface Γ_{sp}. The skeleton of the porous domain is subjected to (i) normal and tangential velocities and stresses due to the coupling to the structure at the interface Γ_{sp} and (ii) the pressure and normal velocity given by the interaction with the acoustic domain at the interface Γ_{pa}. The interstitial fluid in the porous domain is subjected to (i) normal velocities and normal stress due to the coupling to the structure at the interface Γ_{sp} and (ii) the pressure and normal velocity given by the interaction with the acoustic domain at the interface Γ_{pa}. The porosity influences the coupling at the porous-acoustic interface. A thorough description of acoustic behaviour of porous material can be found in [11].

1.2.3 Acoustic part

The acoustic part Ω_a consists of a closed physical boundary Γ_a filled by a fluid, which forms an interior acoustic domain. The acoustic part is subjected (i) to boundary conditions defined at Γ_a and (ii) the normal velocity and pressure distributions at the structural-acoustic interface Γ_{sa} and at the porous-acoustic interface Γ_{pa} accounting for the coupling effects due to the plate dynamics and the coupling to the porous domain respectively. An additional normal velocity boundary condition applied in the acoustic

part at Γ_{sa} accounts for those acoustic-structural coupling effects. The Helmholtz equation is governing the steady-state acoustic pressure perturbation field $p(\mathbf{r})$ in the fluid domain

$$\nabla^2 p(\mathbf{r}) - k^2(\mathbf{r}) = 0, \tag{1.2}$$

where k the acoustic wave number and c the speed of sound [12]. Since we are interested into the stationary response of the system the time dependency $e^{j\omega t}$ will be omitted. The response of the structural-acoustic system is described in terms of steady-state out of-plane displacement w_z (or velocity v) and the acoustic pressure field p.

1.3 Principle of PTF approach

In this section the basics behind the PTF method will be presented, a more detailed and extensive description of the coupling procedure for a generic number of coupled subsystems can be found in [1]. The objective is the reconstruction of the Sound Pressure Level (SPL) at a given position in the acoustic cavity. The PTF is a sub-structuring method. It consists of partitioning of the continuous system into sub-systems and coupling them at their interfaces via impedance or mobility relations. Each interface is subdivided into N elementary surfaces of areas ∂S called patches. For practical reasons the interfaces match with the physical interfaces of the sub-domains. The sub-structuring allows for independent sub-system characterisation. In order to couple the domains a set of transfer function called Patch Transfer Functions (PTF) must be computed. These transfer functions are based on averaged dynamic field quantities on the patches. Once the PTFs are known the coupling procedure consists of the application of the superposition principle. Let us consider an interface S between two sub-domains, and let us divide it into small elementary surfaces S_j, see Fig. 1.2. For the j-th patch centred at position $\mathbf{r}$ of

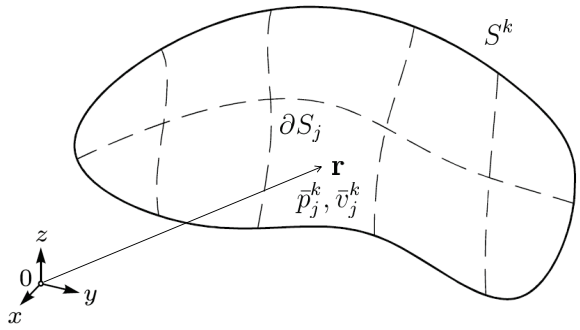

Figure 1.2: Discretisation of the interfaces into patches and assessment of averaged quantities over single patches.

the m-th sub-system the averaged pressure and velocity are given by

$$\bar{p_j^m} = \frac{1}{\partial S} \int_{\partial S_j} p_j^m(\mathbf{r}) dS, \tag{1.3}$$

$$\bar{v_j^m} = \frac{1}{\partial S} \int_{\partial S_j} v_j^m(\mathbf{r}) dS. \tag{1.4}$$

The transfer function between an excited patch j and a receiving patch i defined on the sub-system m can be expressed in terms of impedance by:

$$Z_{ij}^m = \left. \frac{\bar{p}_i^m}{\bar{v}_j^m} \right|_{\bar{v}_{k\neq j}^m = 0}, \tag{1.5}$$

in terms of mobility by:

$$Y_{ij}^m = \left. \frac{\bar{v}_i^m}{\bar{p}_j^m} \right|_{\bar{p}_{k\neq j}^m = 0}. \tag{1.6}$$

To obtain Z_{ij}, we excite with a surface velocity $\bar{v}_j^m$ at a certain patch j and block all other patches so that $\bar{v}_{k\neq j}^m = 0$. Then the i-th row of $\boldsymbol{Z}$ is given by the ratio of all surface pressures to the single velocity, see Eq. (1.5). To determine Y_{ij}, we excite with a surface pressure $\bar{p}_j^m$ at patch j and leave all the other patches free with $\bar{p}_{k\neq j}^m = 0$. The i-th row of $\boldsymbol{Y}$ is given by the ratio of all surface velocities to the single pressure, see Eq. (1.6). The first case will be the natural method for acoustic and porous domains, while the latter for structural ones. In the numerical model, we can just successively apply these boundary conditions to obtain the blocked pressures or free velocities on the surface. In principle this can also be done experimentally, even if the implementation can be difficult. Determination of the impedance and/or mobility matrices is not only restricted to an approach described above, but can be also derived in an indirect manner which is one of the on-going research activities.

In measurements and simulations, the patch transfer functions of a sub-system can be obtained in a straightforward way by splitting the interface into N patches and assuming averaged constant values for the quantities over each patch. The patch values can be obtained by averaging or integrating over measured or simulated quantities inside a patch area. In order to avoid spatial aliasing the sampling spacing has to obey to the Nyquist criterion taking into account the appropriate wavenumber. In order to decide upon the patch discretisation again the Nyquist sampling criterion has to be applied, thus the patch dimension results from $d \leq /k(f_{max})$, see [13]. Following this rules ensure that the radiated sound from the patch discretisation is correctly represented.

1.4 Coupling procedure

The superposition principle is used to couple systems at their common interface. The coupled response of one sub-system is given by the sum of two virtual configurations. In case of a fluid sub-system the two configurations are: the pressure response due to internal sources if the coupled interface is blocked; the pressure response due to the yet unknown interface velocity of the coupled system, when the internal sources are switched off. In case of a structural sub-system the two configurations are: the velocity response

due to internal sources if the coupled interface is free; the velocity response due to the yet unknown interface pressure of the coupled system, when the internal sources are switched off.

1.4.1 Coupling a structural domain with a fluid layer

Let us consider the coupled system in Fig. 1.3 where a thin plate excited by a structural load p^F is coupled to an acoustic rigid cavity. Let $\boldsymbol{Y^S}$ denote the elastic plate mobility,

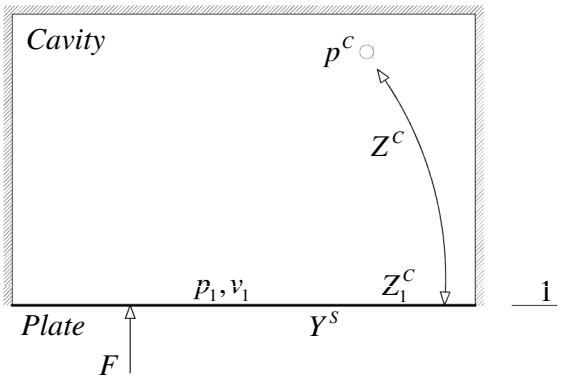

Figure 1.3: A coupled vibro-acousic problem: a structure coupled to a fluid layer.

$\boldsymbol{Z_1^C}$ the cavity surface impedance and $\boldsymbol{p^F}$ the pressure loads vector

$$\boldsymbol{v_1^S} = \boldsymbol{Y^S}\left(\boldsymbol{p_1^S} + \boldsymbol{p^F}\right), \tag{1.7}$$

$$\boldsymbol{p_1^C} = \boldsymbol{Z_1^C}\boldsymbol{v_1^C}. \tag{1.8}$$

$\boldsymbol{Y^S p^F} = \boldsymbol{v_1^S}$ would be the plate response to the force in vacuo ($\boldsymbol{p_1^S} = \boldsymbol{0}$). The continuity conditions for the coupled case, see Fig. 1.4, are

$$\begin{aligned} \boldsymbol{p_1} &= \boldsymbol{p_1^S} = \boldsymbol{p_1^C}, \\ \boldsymbol{v_1} &= \boldsymbol{v_1^S} = \boldsymbol{v_1^C}. \end{aligned} \tag{1.9}$$

Combining Eq. (1.8) and (1.9) yields

$$\boldsymbol{p_1} = \boldsymbol{Z_1^C}\boldsymbol{v_1}. \tag{1.10}$$

The mobility relation Eq. (1.7) yields

$$\boldsymbol{v_1} = \boldsymbol{Y^S}\left(\boldsymbol{p_1} + \boldsymbol{p^F}\right) = \boldsymbol{Y^S}\left(\boldsymbol{Z_1^C}\boldsymbol{v_1} + \boldsymbol{p^F}\right), \tag{1.11}$$

which results in

$$\left(\boldsymbol{I} - \boldsymbol{Y^S Z_1^C}\right) \boldsymbol{v_1} = \boldsymbol{Y^S p^F}. \tag{1.12}$$

The pressure p^C at receiving point is given by

$$p^C = \boldsymbol{(z^C)^T v_1}, \tag{1.13}$$

where $\boldsymbol{(z^C)^T}$ is the transpose of the vector of the acoustic transfer functions between the patches on the interface 1 and the receiving position in the cavity.

1.4.2 Coupling a structural domain with two fluid layers

Let us consider the coupled system in Fig. 1.4 where a thin plate loaded by a point force F is coupled to a fluid layer representing trim, which then couples to an acoustic rigid cavity. The fluid layer is in fact an equivalent fluid used to represent the porous domain. The continuity conditions for pressures and velocities at the interface between

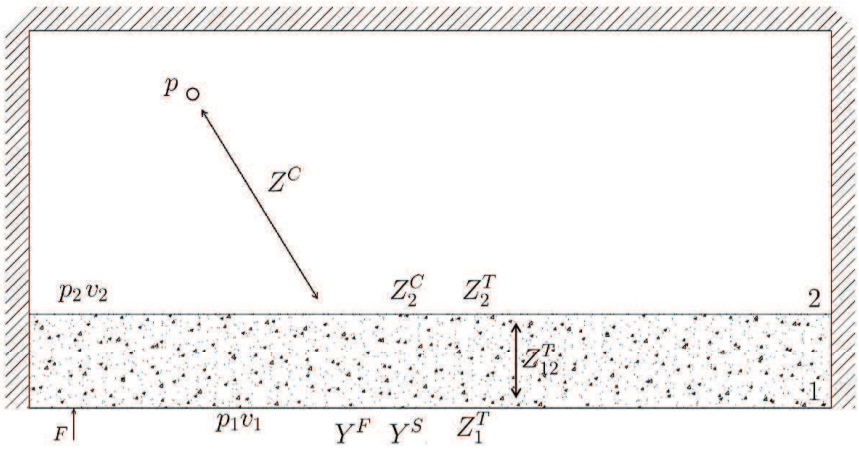

Figure 1.4: A fully coupled vibro-porous-acousic problem: a structure coupled to a poroelastic layer at interface 1 and successively to a fluid layer at interface 2.

the structural and the porous domains are:

$$\begin{aligned} \boldsymbol{p_1} &= \boldsymbol{p_1^S} = \boldsymbol{p_1^T}, \\ \boldsymbol{v_1} &= \boldsymbol{v_1^S} = \boldsymbol{v_1^T}, \end{aligned} \tag{1.14}$$

where the superscript S stands for the structure and T for the trim. Between the porous and the acoustic domains:

$$\begin{aligned} \boldsymbol{p_2} &= \boldsymbol{p_2^T} = \boldsymbol{p_2^C}, \\ \boldsymbol{v_2} &= -\boldsymbol{v_2^T} = \boldsymbol{v_2^C}, \end{aligned} \tag{1.15}$$

where the superscript C stand for the cavity. Between the structural and acoustic domains:

$$\begin{aligned} \boldsymbol{p_1} &= \boldsymbol{p_1^S} = \boldsymbol{p_1^C}, \\ \boldsymbol{v_1} &= \boldsymbol{v_1^S} = \boldsymbol{v_1^C}. \end{aligned} \tag{1.16}$$

The impedance relations at the structure-porous interface write:

$$\boldsymbol{v_1} = \boldsymbol{Y^S p_1} + \boldsymbol{y^F F}, \tag{1.17}$$

$$\boldsymbol{p_1} = \boldsymbol{Z_1^T v1} - \boldsymbol{Z_{12}^T v_2}, \tag{1.18}$$

where $\boldsymbol{Y^S}$ is the mobility matrix of the structure, $\boldsymbol{y^F}$ is a vector of structural transfer function between the point where the load is applied and all patches on the plate. and are the surface trim impedance at interface 1 and the cross trim impedance between interface 1 and 2 respectively. The impedance relations at the acoustic-porous interface write:

$$\boldsymbol{p_2} = \boldsymbol{Z_{12}^T v_1} - \boldsymbol{Z_s^T v_2} = \boldsymbol{Z_2^C v_2}, \tag{1.19}$$

where $\boldsymbol{Z_2^T}$ and $\boldsymbol{Z_2^C}$ are the surface trim impedance and the surface cavity impedance at the interface 2 respectively. The fully coupled problem can be described in a matrix formulation:

$$\begin{pmatrix} \mathbf{1} & -\boldsymbol{Z_1^T} & \boldsymbol{Z_{12}^T} \\ -\boldsymbol{Y^S} & \mathbf{1} & \mathbf{0} \\ \mathbf{0} & \boldsymbol{Z_{21}^T} & \boldsymbol{Z_2^C} \end{pmatrix} \begin{pmatrix} \boldsymbol{v_1} \\ \boldsymbol{p_1} \\ \boldsymbol{v_2} \end{pmatrix} = \begin{pmatrix} \mathbf{0} \\ \boldsymbol{yF} \\ \mathbf{0} \end{pmatrix}. \tag{1.20}$$

Finally the SPL at the receiver position is:

$$\boldsymbol{p} = (\boldsymbol{z^C})^{\boldsymbol{T}}, \tag{1.21}$$

where $(\boldsymbol{z^C})^{\boldsymbol{T}}$ is the transpose of the vector of the acoustic transfer functions between the patches on the interface 2 and the receiving microphone position in the cavity.

Chapter 2

Sampling criterion for structural radiation in fluid

2.1 Introduction

When studying the radiation of sound from vibrating structures, typically, the radiating surface is subdivided into finite-sized elemental areas, in which the surface vibrations is considered uniform over the element area. In order to do this, the size of these elemental areas, here also referred as patches, has to be chosen. If the vibration field is sampled according to the acoustic Nyquist sampling criterion, taking into account the acoustic wavelength only, then spatial aliasing will occur if the structural wavelength is shorter than the acoustic wavelength. Problems will thus occurs below coincidence which is the frequency range addressed in this chapter.

Holland et al. [13, 14] suggested that the acoustic Nyquist criterion could also be used below coincidence provided area-averaged complex patch velocities were used. They argued that the structural wave components with wavenumbers greater than the acoustic wavenumber would tend to be averaged out, leaving only those components that contribute significantly to the radiated sound. No rigorous analysis was given but some numerical examples were provided for a baffled simply supported rectangular plate showing encouraging results supporting the idea.

In the present work the above mentioned area-averaged sampling scheme is analysed more in depth for a simply supported baffled plate radiating into semi-infinite fluid. Analytical closed form expressions are derived for the frequency band averaged velocities and structural wavelengths resulting from the sampling. The variations of the velocities and of the radiation efficiencies turn out to balance each other resulting in a minor variation of the radiated power in the valid frequency range [15].

First the theory is presented, proving that a patch discretised system can, in an average sense, be represented by an equivalent, frequency independent, structural wavelength equal to roughly 2.3 times the patch size. Next, a simple analytical model for the average radiation efficiency is proposed based on earlier publications. A novel analytical model for the description of the average square velocity of a simply supported plate

discretised into patches is presented. The proposed models are compared to numerical investigation. Finally, the presented results are discussed.

2.2 Average patch wavelength

2.2.1 The area-averaged wavelength: the one dimensional case

In order to clarify the different concepts the simple one dimensional case is briefly addressed. Consider a plane transverse wave with structural wavenumber $k_s = 2\pi/\lambda_s$ propagating along the surface of a plate in the positive x direction with velocity

$$v(x,t) = \hat{v}e^{-i(k_s x - \omega t)}, \tag{2.1}$$

where ω is the radian frequency. In the following the time dependence is omitted for

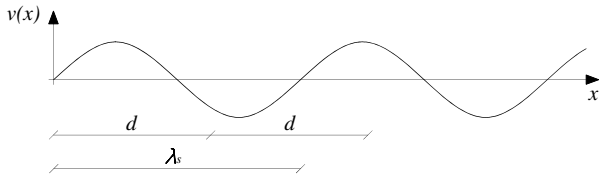

Figure 2.1: Plane wave propagating in the x-direction, patch size d.

the sake of brevity. If patches of size $d \times d$ are assumed, see Fig. 2.1, the area-averaged velocity, hereafter referred to as *patch velocity*, of the r-th patch may be written as

$$\langle v \rangle_r = \frac{1}{d}\int_{(r-1)d}^{rd} \hat{v}e^{-ik_s x}dx = \frac{j\hat{v}}{k_s d}e^{-jk_s dr}\left(1 - e^{jk_s d}\right), \tag{2.2}$$

where the $\langle\cdot\rangle$ sign is used to indicate a spatial average. The ratio between the velocities of two neighbouring patches is given by

$$\frac{\langle v \rangle_r}{\langle v \rangle_{r-1}} = e^{-jk_s d}, \tag{2.3}$$

resulting in a structural wavelength λ_p of the patch plate (normalised with respect to d) hereafter referred to as patch wavelength

$$\frac{\lambda_p}{d} = \left|\frac{2\pi}{arg\left(e^{-jk_s d}\right)}\right|. \tag{2.4}$$

In Fig. 2.2 an example is given. The original and the area-averaged vibration fields for $d = 1.1\lambda_s$ are illustrated for $t = \pi/2\omega$ and $t = \pi/2\omega + \pi/4\omega$ respectively. The area averaging results in a low amplitude propagating wave with wavelength of $10d$. The normalised structural wavelength and patch wavelength are displayed in Fig. 2.3. For

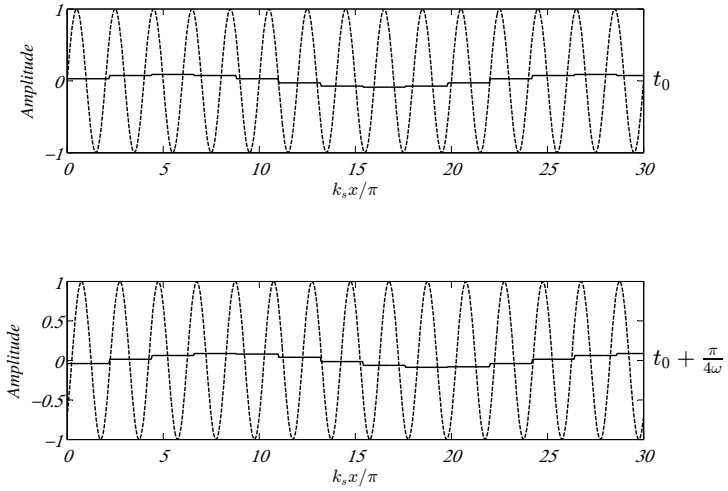

Figure 2.2: Actual vibration field (dashed line) compared to the corresponding area averaged field (solid line).

$k_s d \leqslant \pi$, that is, until the structural Nyquist criterion is met, the wavelength of the patch plate corresponds with the structural wavelength. For $k_s d > \pi$, the structural wavelength keeps on decreasing with increasing $k_s d$ whereas, the patch wavelength oscillates between $2d$ (smaller wavelengths cannot be represented) and infinity when all the patches result in phase.

2.2.2 The area-averaged wavelength: the bi-dimensional case

Each of the transverse vibration mode shapes of a rectangular simply supported plate consist of the superposition of two couples of plane waves propagating back and forth under two well defined angles. For the assessment of the patch wavelength it is therefore sufficient to consider the single traveling wave pattern on a finite rectangular structural domain propagating in direction α with wavenumbers $k_x = k_s cos\alpha$, $k_y = k_s sin\alpha$ and with amplitude $\hat{v}$

$$v\left(x,y\right) = \hat{v}e^{-jk_x x}e^{-jk_y y}. \tag{2.5}$$

The radiation efficiency of the plane propagating wave pattern of Eq. (2.5) on a finite rectangular baffled domain may be obtained using the spatial windowing technique presented by Villot et al. [16] and later in a simplified version by Vigran [17]. The latter showed that a good approximation for the radiation efficiency could be obtained by the

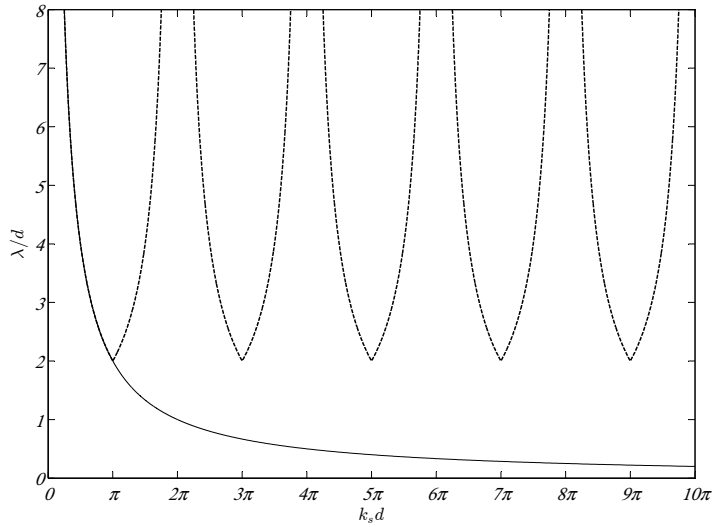

Figure 2.3: The normalised structural (solid line) and patch (dashed line) wavelength, Eq. (2.4), of a one dimensional system.

following expression:

$$\sigma(k_s) = \frac{k_0\sqrt{S}}{2\pi}\int_0^{k_0} \frac{sin^2\left[(k_r - k_s)\frac{\sqrt{(S)}}{2}\right]}{\left[(k_r - k_s)\frac{\sqrt{(S)}}{2}\right]^2\sqrt{k_0^2 - k_r^2}}dk_r \tag{2.6}$$

where k_0 is the wavenumber in air, S the surface of the plate and k_r the spatial transform wavenumber. This integral cannot be evaluated in closed form but well below coincidence, $(k_s \gg k_r)$ the following approximation can be obtained

$$\sigma(k_s) = \frac{k_0\sqrt{S}}{2\pi}\frac{2}{k_s^2 S}\int_0^{k_0}\frac{1}{\sqrt{k_0^2 - k_r^2}}dk_r = \frac{k_0}{2\sqrt{S}k_s^2}. \tag{2.7}$$

The radiated power consequently turns out to be proportional to $(\lambda_s v)^2$. The area-averaged patch velocity of the q, r patch is given by

$$\begin{aligned}\langle v\rangle_{q,r} &= \frac{1}{d^2}\int_{(q-1)d}^{qd}\int_{(r-1)d}^{rd}\hat{v}e^{-ik_x x}e^{-ik_x x}dxdy \\ &= \frac{2\hat{v}}{j^2k_s^2d^2sin\,(2\alpha)}e^{-jk_s dqcos(\alpha)}\left(e^{jk_s dcos(\alpha)} - 1\right) \\ &\quad e^{-jk_s drsin(\alpha)}\left(e^{jk_s dsin(\alpha)} - 1\right).\end{aligned} \tag{2.8}$$

The indexes q and r are associated with the patch position, see Fig. 2.4. The phase be-

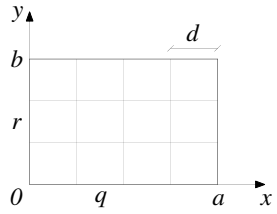

Figure 2.4: Definition of a parametric coordinate system for the patch-plate.

tween the velocities of two neighbouring patches in the x and y direction is consequently given by

$$\frac{\langle v\rangle_{q,r}}{\langle v\rangle_{q-1,r}} = e^{-jk_s dcos\alpha}, \tag{2.9}$$

$$\frac{\langle v\rangle_{q,r}}{\langle v\rangle_{q,r-1}} = e^{-jk_s dsin\alpha}, \tag{2.10}$$

and the projections of the patch wavelength in $x-$ and $y-$direction become

$$\lambda_{p,x}\left(k_s,\alpha\right) = \left|\frac{2\pi d}{arg\left(e^{-jk_s dcos\alpha}\right)}\right|, \tag{2.11}$$

$$\lambda_{p,y}\left(k_s,\alpha\right) = \left|\frac{2\pi d}{arg\left(e^{-jk_s dsin\alpha}\right)}\right|. \tag{2.12}$$

The spatial patch averaging creates a propagating wave in a direction which is not necessarily corresponding with the one of the original field, depending whether the Nyquist structural criterion is satisfied or not in one or both $x-$ and $y-$projections. By recalling the well known relation between the structural wavenumber and the components in the $x-$ and $y-$directions

$$k_s^2 = k_x^2 + k_y^2, \tag{2.13}$$

Eq. (2.13) may be re-written in terms of λ_s

$$\lambda_s = \sqrt{\frac{\lambda_x^2\lambda_y^2}{\lambda_x^2+\lambda_y^2}}. \tag{2.14}$$

The normalised patch wavelength is obtained by substituting Eq. (2.11) and (2.12) into (2.14)

$$\frac{\lambda_p\left(k_s,\alpha\right)}{d} = 2\pi\sqrt{\frac{1}{\left|arg\left(e^{-jk_s dcos\alpha}\right)\right|^2 + \left|arg\left(e^{-jk_s dsin\alpha}\right)\right|^2}}. \tag{2.15}$$

Closer inspection reveals that λ_p/d reaches the minimum value of $\sqrt{2}$ each time the projection of the structural half-waves on the x-and y-axis exactly fit an odd-integer times into the patch size d. Furthermore the function has isolated singularities each time the

patch size corresponds with even-integer multiples of the wavelength projections. Close to the singularities the function tends to infinity.

The λ_p/d function is not, as usual, proportional with some power of the frequency but instead constantly oscillates between $\sqrt{2}$ and infinity depending on the structural wavelength and the propagation angle of the original field. It is therefore meaningful to investigate whether it is possible to define a constant average value which would be representative for broad band applications characterised by the superposition of many plane waves propagating in different directions with different wavelengths, as would be the case for broad band excited finite rectangular plates. The straightforward average over a sufficient large $k_s d$ range leads to the following expression

$$\frac{\langle \lambda_p(\alpha) \rangle}{d} = \frac{1}{(k_s d)_2 - (k_s d)_1} \int_{(k_s d)_1}^{(k_s d)_2} \frac{\lambda_p}{d} d(k_s d). \tag{2.16}$$

where $(k_s d)_1 = \pi$, corresponding to structural aliasing, and $(k_s d)_2 = n\pi$ with $n \gg 1$. This integral cannot be evaluated analytically and exhibits numerical convergence problems caused by the singularities. However, at the singularities where the wavelength tends to infinity the patch velocity, Eq. (2.8), goes to zero and no power is radiated. The singularities are consequently not very important from the point of view of the radiated power. Since the power radiated by a plane propagating wave of a baffled rectangular domain is proportional to the product of velocity and wavelength, see Eq. (2.7), it is meaningful to calculate a weighted $k_s d$ average of the wavelength with the velocity as a weight function

$$\frac{\langle \lambda_p(\alpha) \rangle}{d} = \frac{\int_{(k_s d)_1}^{(k_s d)_2} \frac{\lambda_p}{d} |v_p| \, d(k_s d)}{\int_{(k_s d)_1}^{(k_s d)_2} |v_p| \, d(k_s d)}. \tag{2.17}$$

The weighting renders the integrand well-behaved eliminating the singularities and poses no significant stability problems. The results turns out to be almost independent on the upper limit of integration as long as a sufficient number of oscillations are included in the integration interval. The outcome of the numerical integration is shown in Fig. 2.5. The patch wavelength is roughly $4d$ for $\alpha = 0$ and $\pi/2$, and it becomes close to $2d$ for $\alpha = \pi/4$.

Furthermore, we may average over all possible direction of propagation $\alpha \in [0, \pi/2]$

$$\frac{\langle\langle \lambda_p \rangle\rangle}{d} = \frac{2}{\pi} \int_0^{\pi/2} \frac{\langle \lambda_p(\alpha) \rangle}{d} d\alpha \simeq 2.3. \tag{2.18}$$

The results of this average indicates an equivalent, frequency and propagation direction averaged, wavelength for the patch plate equal to 2.3 times the patch size.

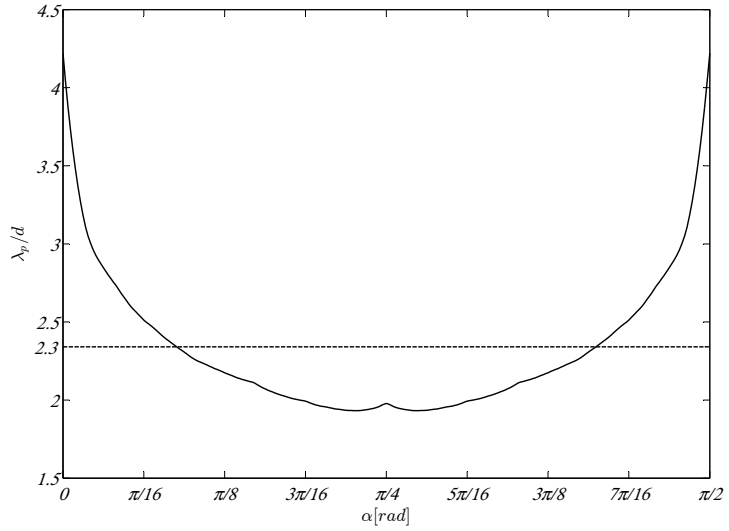

Figure 2.5: The normalised, frequency averaged, patch wavelength $\langle \lambda_p(\alpha) \rangle / d$ as a function of the direction of propagation (solid line) and its average $\langle\langle \lambda_p \rangle\rangle / d$ over all directions of propagation (dashed line).

2.3 Derivation of the mean square patch velocity

The objective of this section is the assessment of the averaged square velocity of a point excited thin plate with simply supported boundary conditions and of its patch discretisation.

2.3.1 Plate

Let us consider a thin plate made of an homogeneous elastic material with damping loss factor η and excited by a point force F. The mean square velocity normal to the surface averaged over all possible excitation positions is given by Cremer et al. [18]

$$\overline{\langle\langle v^2 \rangle\rangle} = \frac{F^2}{S^2 \overline{m}^2} \frac{\pi}{2\eta\omega} \frac{\Delta N}{\Delta\omega}, \tag{2.19}$$

where $\overline{m}$ the mass per unit area and $\frac{\Delta N}{\Delta\omega}$ the modal density for a uniform plate in bending. We may write the modal density as $\frac{k_s^2 S}{4\pi\omega}$, thus the mean square average velocity in a frequency band $\Delta\omega$ due to a broadband structural excitation F_Δ becomes

$$\overline{\langle\langle v(x,y)^2 \rangle\rangle}\Big|_{\triangle\omega} = \frac{F_\triangle^2 k_s^2}{8 S \overline{m}^2 \omega^2 \eta}. \tag{2.20}$$

This velocity response is independent of the boundary conditions, and it is a function of the surface, the mass per unit area, the angular frequency, the loss factor and of the

bending wavenumber.

2.3.2 Patch-plate

The vibration field of a plate can be expressed as a sum of eigenfunctions

$$v(x,y) = \sum_{m=1}^{\infty}\sum_{n=1}^{\infty} v_{m,n}\varphi_{m,n}(x,y), \tag{2.21}$$

where $\varphi_{m,n}(x,y)$ represent the shape functions. For the case of a thin simply supported plate made of homogeneous linear-elastic material, in presence of damping, excited by a pressure distribution the amplitudes of the modal velocities are given by

$$v_{m,n} = \frac{j\omega}{\left[\omega_{m,n}^2\left(1+j\eta\right)-\omega^2\right]\Lambda_n}\int_{S_0} p(x,y)\varphi_{m,n}(x,y)dS. \tag{2.22}$$

The shape functions can be written as

$$\varphi_{m,n}(x,y) = sin\left(\frac{m\pi}{a}x\right)sin\left(\frac{n\pi}{b}y\right), \tag{2.23}$$

where a, b are the plate dimensions in the $x-$ and $y-$directions respectively and m, n the mode counters. Moreover, the norm can be written as

$$\Lambda_{m,n} = \int_S \overline{m}\varphi_{m,n}(x,y)^2 dS = \overline{m}S/4. \tag{2.24}$$

In case of point force applied on a infinitesimally small area at the position x_0, y_0 one may write $\int p(x_0,y_0)dx_0dy_0 = F(x_0,y_0)$ and assume $\varphi_{m,n}(x,y)$ constant over the integration region, therefore Eq. (2.22) becomes

$$v_{m,n} = \frac{j\omega}{\left[\omega_{m,n}^2\left(1+j\eta\right)-\omega^2\right]\Lambda_n}F(x_0,y_0)\varphi_{mn}(x_0,y_0). \tag{2.25}$$

Combining Eq. (2.21), (2.24) and (2.25) leads to

$$v(x,y) = \sum_{m=1}^{\infty}\sum_{n=1}^{\infty}\frac{4j\omega F(x_0,y_0)}{\left[\omega_{m,n}^2\left(1+j\eta\right)-\omega^2\right]\overline{m}S}\varphi_{m,n}(x,y)\varphi_{m,n}(x_0,y_0). \tag{2.26}$$

Eq. (2.26) is the eigenfunctions expansion theorem applied to a simply supported plate. In order to be general one may average over all possible excitation positions instead of dealing with a specific force location, obtaining

$$\begin{aligned}\left\langle v\left(x,y\right)\right\rangle =& \frac{1}{S}\int_S\sum_{m=1}^{\infty}\sum_{n=1}^{\infty}\frac{4j\omega F}{\left[\omega_{m,n}^2\left(1+j\eta\right)-\omega^2\right]\overline{m}S}\varphi_n(x,y)\\ &\left|\varphi_{m,n}(x_0,y_0)\right|dx_0dy_0.\end{aligned} \tag{2.27}$$

Eq. (2.27) results in

$$\langle v\left(x,y\right)\rangle = \sum_{m=1}^{\infty}\sum_{n=1}^{\infty} \frac{j\omega}{\left[\omega_{m,n}^2\left(1+j\eta\right)-\omega^2\right]} \frac{16F}{\pi^2\overline{m}S}\varphi_n(x,y)dS. \tag{2.28}$$

As was already mentioned in the introduction the velocity of the $i-$th patch $v_{p,i}$ is obtained by averaging the complex velocity over the patch surface

$$v_{p,i} = \frac{1}{S_p}\int_{S_p} \langle v\left(x,y\right)\rangle \, dxdy. \tag{2.29}$$

The average squared velocity of the patch-plate is given by

$$\left\langle \langle v\rangle^2 \right\rangle = \frac{1}{N_p}\sum_{i=1}^{Np} \left|v_{p,i}\right|^2, \tag{2.30}$$

where N_p is the total number of patches. Substitution of Eq. (2.28) and (2.29) in Eq. (2.30) yields

$$\begin{aligned}\left\langle \langle v\rangle^2 \right\rangle =& \frac{1}{N_p}\sum_{q}^{N_{px}}\sum_{r}^{N_{py}} \left| \frac{1}{d^2}\int_{(q-1)d}^{qd}\int_{(r-1)d}^{rd} \sum_{m=1}^{\infty}\sum_{n=1}^{\infty} \right. \\ & \left. \frac{j\omega}{\left[\omega_{m,n}^2\left(1+j\eta\right)-\omega^2\right]} \frac{16F}{\pi^2\overline{m}S}\varphi_{m,n}(x,y)dxdy \right|^2.\end{aligned} \tag{2.31}$$

where $N_{px} = a/d$ and $N_{py} = b/d$ are the number of patches in the x and y direction respectively. The indexes q and r are associated with the patch position, see Fig. 2.4. If, analogous to section 2.3.1 broadband excitation F_Δ is assumed the band averaged mean square velocity may be obtained as

$$\begin{aligned}\overline{\left\langle \langle v\rangle^2 \right\rangle}_{\Delta\omega} =& \frac{1}{\Delta\omega}\int_{\Delta\omega} \frac{1}{N_p}\sum_{q}^{N_{px}}\sum_{r}^{N_{py}} \left| \frac{1}{d^2}\int_{(q-1)d}^{qd}\int_{(r-1)d}^{rd} \sum_{m(N_1)}^{m(N_2)}\sum_{n(N_1)}^{n(N_2)} \right. \\ & \left. \frac{j\omega}{\left[\omega_{m,n}^2\left(1+j\eta\right)-\omega^2\right]} \frac{16F_\Delta}{\pi^2\overline{m}S}\varphi_{m,n}(x,y)dxdy \right|^2 d\omega.\end{aligned} \tag{2.32}$$

The modal summation is now performed between the lowest and the highest mode inside the frequency band $\Delta\omega$, $m(N_1, n(N_1)$ and $m(N_2, n(N_2)$ respectively. The integral of the sum over the modes can be replaced by the sum of the integrals over the single modes.

In this way the mode order m, n is constant inside the integral.

$$\begin{aligned}\overline{\left\langle \langle v \rangle^2 \right\rangle}_{\Delta\omega} =& \frac{1}{\Delta\omega}\frac{1}{N_p}\sum_{q}^{N_{px}}\sum_{r}^{N_{py}}\left|\frac{1}{d^2}\int_{(q-1)d}^{qd}\int_{(r-1)d}^{rd}\sum_{m(N_1)}^{m(N_2)}\sum_{n(N_1)}^{n(N_2)}\right. \\ & \left.\int_{\Delta\omega}\frac{j\omega}{\left[\omega_{m,n}^2\left(1+j\eta\right)-\omega^2\right]}d\omega\frac{16F_\Delta}{\pi^2\overline{m}S}\varphi_{m,n}(x,y)dxdy\right|^2 .\end{aligned} \tag{2.33}$$

The integration over frequency bands can be approximated by $\frac{\pi}{2\eta\omega_{m,n}}$, [18]. The remainder of the integration, that is the contribution of the modes outside the frequency band of excitation, has been neglected. If we approximate $\omega_{m,n}$ constant within each frequency and replace it by the centre frequency band $\omega_{mc,nc}$ of the band under consideration the following is obtained

$$\begin{aligned}\overline{\left\langle \langle v \rangle^2 \right\rangle}_{\Delta\omega} =& \frac{\Delta N}{\Delta\omega}\frac{16^2F_\Delta^2}{\pi^4\overline{m}^2S^2}\frac{\pi}{2\eta\omega_{mc,nc}} \\ & \frac{1}{N_p}\sum_{q}^{N_{px}}\sum_{r}^{N_{py}}\left|\frac{1}{d^2}\int_{(q-1)d}^{qd}\int_{(r-1)d}^{rd}\sum_{m(N_1)}^{m(N_2)}\sum_{n(N_1)}^{n(N_2)}\varphi_{m,n}(x,y)dxdy\right|^2 ,\end{aligned} \tag{2.34}$$

where ΔN is the number of resonance frequencies inside the frequency band $\Delta\omega$. Eq. (2.34) can be re-written as

$$\begin{aligned}\overline{\left\langle \langle v \rangle^2 \right\rangle}_{\Delta\omega} =& \frac{\Delta N}{\Delta\omega}\frac{16^2F_\Delta^2}{\pi^4\overline{m}^2S^2}\frac{\pi}{2\eta\omega_{mc,nc}} \\ & \frac{1}{N_p}\sum_{q}^{N_{px}}\sum_{r}^{N_{py}}\left|\frac{1}{d^2}\sum_{m(N_1)}^{m(N_2)}\sum_{n(N_1)}^{n(N_2)}\int_{(q-1)d}^{qd}\int_{(r-1)d}^{rd}\varphi_{m,n}(x,y)dxdy\right|^2 .\end{aligned} \tag{2.35}$$

The integration over the patch surface results in

$$\begin{aligned}\overline{\left\langle \langle v \rangle^2 \right\rangle}_{\Delta\omega} =& \frac{\Delta N}{\Delta\omega}\frac{16^2F_\Delta^2}{\pi^4\overline{m}^2S^2}\frac{\pi}{2\eta\omega_{mc,nc}}\frac{1}{N_p}\sum_{q}^{N_{px}}\sum_{r}^{N_{py}}\left|\frac{1}{d^2}\sum_{m(N_1)}^{m(N_2)}\sum_{n(N_1)}^{n(N_2)}\right. \\ & \frac{S}{mn\pi^2}\left[cos\left(\frac{m\pi}{N_{px}}\left(q-1\right)\right)-cos\left(\frac{m\pi}{N_{px}}q\right)\right] \\ & \left.\left[cos\left(\frac{n\pi}{N_{py}}\left(r-1\right)\right)-cos\left(\frac{n\pi}{N_{py}}r\right)\right]\right|^2 .\end{aligned} \tag{2.36}$$

The term $\frac{1}{m^2n^2}$ is assumed constant inside the frequency band and can be moved outside the summation. By observing Eq. (2.36) one may define

$$\begin{aligned} C^2 =& \frac{1}{N_p} \sum_{q}^{N_{px}} \sum_{r}^{N_{py}} \left| \sum_{m(N_1)}^{m(N_2)} \sum_{n(N_1)}^{n(N_2)} \left[cos\left(\frac{m\pi}{N_{px}} (q-1) \right) - cos\left(\frac{m\pi}{N_{px}} q \right) \right] \right. \\ & \left. \left[cos\left(\frac{n\pi}{N_{py}} (r-1) \right) - cos\left(\frac{n\pi}{N_{py}} r \right) \right] \right|^2 . \end{aligned} \tag{2.37}$$

C^2 is dependent on the modes shapes (and consequently the aspect ratio of the plate) and on the patch discretisation scheme. The average value of C^2 will be assessed at the end of this section.

The relation between the mode orders and the structural wavenumber is:

$$k_s^2 = k_x^2 + k_y^2 = k_s^2 cos^2\alpha + k_s^2 sin^2\alpha = \left(\frac{m\pi}{a} \right)^2 + \left(\frac{n\pi}{b} \right)^2 ,$$

therefore

$$mn = \frac{ab}{\pi^2} k_s^2 cos\left(\alpha\right) sin\left(\alpha\right) = \frac{S}{\pi^2} k_s^2 \frac{1}{2} sin\left(2\alpha\right) .$$

In case of an isotropic plate with high modal density adjacent values of m, n are very close to each other and mn may be considered as a continuous function in the wavenumber space. The average of the function mn over a frequency band $2\Delta k_s$ and over the angle $\alpha \in [0 - \pi/2]$ in the k_x, k_y space is

$$\begin{aligned} \overline{mn} &= \frac{1}{\frac{\pi}{4}\left(k_2^2 - k_1^2\right)} \int_{k_1}^{k2} \int_{\alpha_1}^{\alpha_2} \frac{k_s^2 S}{\pi^2} \frac{sin(2\alpha)}{2} k_s dk_s d\alpha \\ &= \frac{S k_s^2}{\pi^3} \left[1 + \left(\frac{\Delta k_s}{k_s} \right)^2 \right] \\ &\cong \frac{S k_s^2}{\pi^3} . \end{aligned} \tag{2.38}$$

In Figure 2.6 mn is shown as a function of the resonance frequencies for an aluminium plate of dimension $1m$, $0.8m$ and $5mm$ thickness. Assuming mn as a continuous function of the frequency gives an excellent approximation of the frequency band averaged mn. Since the velocity is averaged assuming the k_s as a continuous functions of ω and α it may be conclude that the averaging process takes into account all the possible aspect ratio's of a panel of given material properties and thickness. Substituting Eq. (2.38) in (2.36) yields

$$\overline{\left\langle \langle v \rangle^2 \right\rangle}_{\Delta\omega} = \frac{\Delta N}{\Delta\omega} \frac{16^2 F_\Delta^2}{\pi^4 \overline{m}^2 S^2} \frac{\pi}{2\eta\omega_{mc,nc}} \frac{N_p^2}{\pi^4} \frac{\pi^6}{k_s^4 S^2} C^2 . \tag{2.39}$$

One may re-write $\frac{\Delta N}{\Delta\omega}$ as the modal density of a homogeneous plate in bending $\frac{k_s^2 S}{4\pi\omega}$ [18]

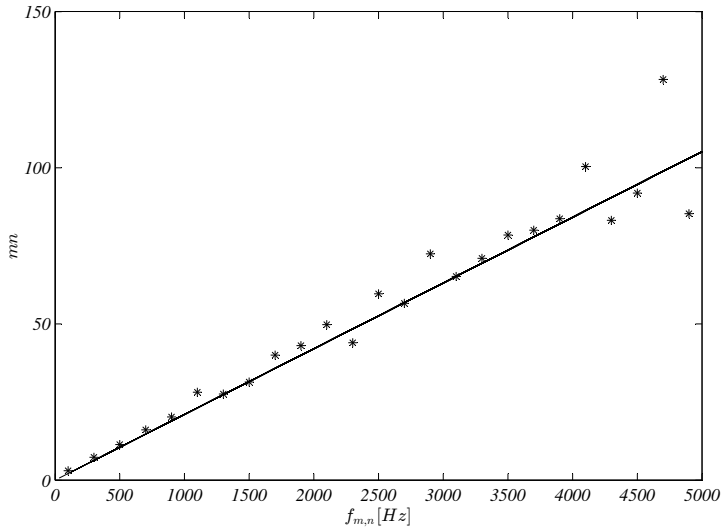

Figure 2.6: frequency band average mn (markers) as a function of the natural frequencies of an aluminium plate of dimensions 1.0 m, 0.8 m and 5mm thick compared to Eq. (2.38) (solid line) where mn is considered as a continuous function of the frequency .

resulting in

$$\overline{\left\langle \langle v \rangle^2 \right\rangle}_{\Delta\omega} = \frac{32 F_\Delta^2 N_p^2 C^2}{\eta \pi^2 \overline{m}^2 \omega^2 k_s^2 S^3}. \tag{2.40}$$

The frequency band averaged patch velocity turns out to be a function of the material properties, the surface, the number of patches, the angular frequency, the damping and the amplitude of the excitation.

In Fig. 2.7 the dispersion curves of the plate, the patch-plate and the fluid are shown. The coincidence frequency of the plate is located at the intersection between the acoustic and the structural wavenumber, k_0 and k_s. For $f \leq f_{N,s} = 2\pi/\lambda_p^2\sqrt{(D/\overline{m})}$ the patch-plate wavenumber k_p is equal to the one of the actual plate. For $f > f_{N,s}$ the structural Nyquist sampling criterion is disobeyed and spatial averaging over patches results in an aliasing mechanism. The structural wavenumber is mirrored respect to k_p resulting in its alias k_s'. The patch-plate wavenumber k_p is, on average, described by a constant wavelength equals to $2.3d$ and the actual plate wavenumber cannot be represented. The intersection between the acoustic and the patch-plate wavenumber represents the patch-plate coincidence frequency, or, in other words, the acoustic Nyquist sampling criterion $f_{cp} = f_{N,0} = c_0/2.3d$.

The plate and patch-plate velocity curves, Eqs. (2.20) and (2.40) respectively, must necessarily intersect for $k_s = k_p = 2\pi/\lambda_p$ and consequently the average constant $\overline{C^2}$ results in

$$\overline{C^2} = \frac{\pi^6}{16\left(\frac{\lambda_p}{d}\right)^4} = 2.147. \tag{2.41}$$

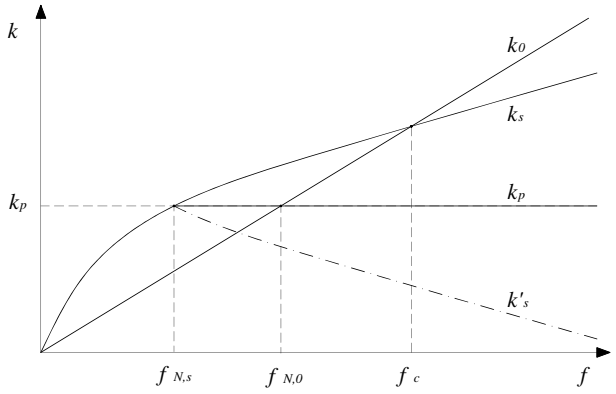

Figure 2.7: Aliasing mechanism in wavenumber space. k_0 is the acoustic wavenumber, k_s is the structural wavenumber, k_p is the patch-plate wavenumber and k'_s is the aliased structural wavenumber.

The patch-plate mean square velocity is given by Eq. (2.20) and by Eq. (2.40) respectively below and above the structural Nyquist limit $f_{N,s}$

$$\overline{\left\langle \langle v \rangle^2 \right\rangle}_{\Delta\omega} = \begin{cases} \frac{F_{\triangle}^2 k_s^2}{8S\overline{m}^2\omega^2\eta}, & \text{for } f \leq f_{Ns} \\ \frac{32F_{\triangle}^2 N_p^2 \overline{C^2}}{\eta\pi^2\overline{m}^2\omega^2 k_s^2 S^3}, & \text{for } f > f_{Ns}. \end{cases} \tag{2.42}$$

2.4 Modal average radiation efficiency

Among others Leppington et al. [19] solved the integral equations for the radiation efficiency. An asymptotic modal solutions for different wavenumber space regions is presented in that work and, based on these results, a modal average radiation efficiency over frequency bands for the case of simply supported isotropic plates is introduced. As for the velocity, the radiation efficiency is averaged assuming k_s as a continuous functions in the wavenumber space. A normalised structural wavenumber is defined as

$$\mu_s = \frac{k_s}{k_0}. \tag{2.43}$$

As discussed in the previous section, in case of the patch-plate we may assume an average wavenumber given by $k_p = 2\pi/\lambda_p$, where $\lambda_p = 2.3d$. The patch coincidence frequency will occurs at $c_0/2.3d$. Therefore for the patch-plate

$$\mu_p = \begin{cases} \frac{k_s}{k_0}, & \text{for } f \leq f_{Ns} \\ \frac{k_p}{k_0}, & \text{for } f > f_{Ns}. \end{cases} \tag{2.44}$$

We may consider the modal average solution proposed by Leppington et al. [19] and we may apply Eq. (7.6), (7.7) and (7.9) of that work to a plate and to the corresponding patch-plate. Above coincidence, $\mu_i < 1$, the average radiation efficiency is given by

$$\overline{\sigma}_i = \frac{1}{\sqrt{1-\mu_i^2}}. \tag{2.45}$$

The validity of Eq.(2.45) requires $k_0 L_{min}(1-\mu_i)$ to be large, where $L_{min} = min\{a, b\}$. Below coincidence, $\mu_i > 1$, the average radiation efficiency is

$$\overline{\sigma}_i = \frac{a+b}{\pi \mu_i k_0 ab\sqrt{\mu_i^2-1}} \left[ln\left(\frac{\mu_i+1}{\mu_i-1}\right) + \frac{2\mu_i}{\mu_i^2-1} \right], \tag{2.46}$$

which requires $k_0 L_{min}(1-\mu_i) \gg 1$. At coincidence the average radiation efficiency is given by

$$\overline{\sigma}_i = \sqrt{k_0 L_{min}} H(l), \tag{2.47}$$

where l is the aspect ratio of the panel. The function $H(l)$ is chosen based on the aspect ratio of the plate [19], a good approximation is given by $H = 0.5$. The average radiation efficiency of the plate and the corresponding patch-plate is given by Eqs. (2.45-2.47) where μ_i is substituted by μ_s in case of the plate and by μ_p in case of the patch-plate. Although the vibration mode shapes of a simply supported plate do not necessary match those of the associated patch-plate, it is assumed that the two plates show equivalent radiation efficiency when averaged over frequency bands containing many modes. It is, in other words, assumed that Leppington's formula can also be used for the patch-plate.

2.5 Numerical investigations

The presented analytical formulation has been validated by means of numerical modelling. The numerically determined acoustic power radiated by a baffled plate has been compared to the one of the corresponding patch-plate. First, a coupled structural-acoustic FE model of a simply supported panel in a rigid baffle radiating into an hemispheric space has been used to determine the plate structural velocity field and the acoustic power radiated. The plate and the fluid domain were modelled by shell and solid elements respectively. Perfectly Matched Layer type of boundary conditions were used in order to avoid reflections at the outer boundary of the fluid mesh. A point force has been placed close to the centre of the panel in order to efficiently excite low order plate modes. The average square velocity of the plate has been determined. The radiated sound power has been calculated at the outer boundary of the fluid mesh. In a second step the radiated acoustic power of the patch-plate has been determined by means of an acoustic FE model. An hemispheric fluid space has been modelled and, in order to represent the patch-plate velocity field, velocity type of boundary conditions have been used. At each patch the corresponding phase-averaged velocity has been assigned. A

Perfectly Matched Layer has been implemented at the curved part of the hemispheric boundary such that no energy was reflected back. In order to model a rigid baffle the remaining part of the domain has been blocked. The power radiated by the patch-plate has been computed and compared with the one of the original structure. This procedure has been carried out for a plate which details are specified in table 2.1.

$a\ [m]$	1.0
$b\ [m]$	0.8
$t\ [m]$	0.005
$\rho\ [kg/m^3]$	2700
$E\ [Pa]$	$70e^9$
ν	0.3
η	0.01
$d\ [m]$	0.20

Table 2.1: Properties of the panel used in the numerical investigation.

2.5.1 Averaged square velocity

In Fig. 2.8 a comparison between the average square velocity of a plate and the associated patch-plate is shown. The averaged velocity is determined, for both systems, by means of the analytical models presented in Section 2.3 and compared to the corresponding FE numerical model. For the plate considered in this example the structural Nyquist sampling criterion is disobeyed for $f \geqslant 300Hz$. The analytical plate and the patch-plate models intersect at $f = 230Hz$. Once the structural Nyquist sampling criterion is disobeyed the average square velocity of the patch-plate is significantly reduced by the averaging process. The average trends of the plate and associated patch-plate are indeed well approximated by the analytical expressions (2.20) and (2.42).

2.5.2 Radiation efficiency

A comparison between the numerically computed radiation efficiencies and the analytical models presented in Section 2.4 is shown in Fig. 2.9. In both cases an adequate prediction can be observed. The Leppington model gives a good estimation of the average radiation efficiency of the patch-plate. In the low frequency range, below $150Hz$, both analytical models diverge from the numerical curves. This can be attributed to a poor modal density of the plate considered in the numerical investigation and to the fact that the response was not averaged over different excitation position.

2.6 Sound power

The average square velocity and radiation efficiency can be combined in order to determine the acoustic power radiated by a simply supported plate and its corresponding

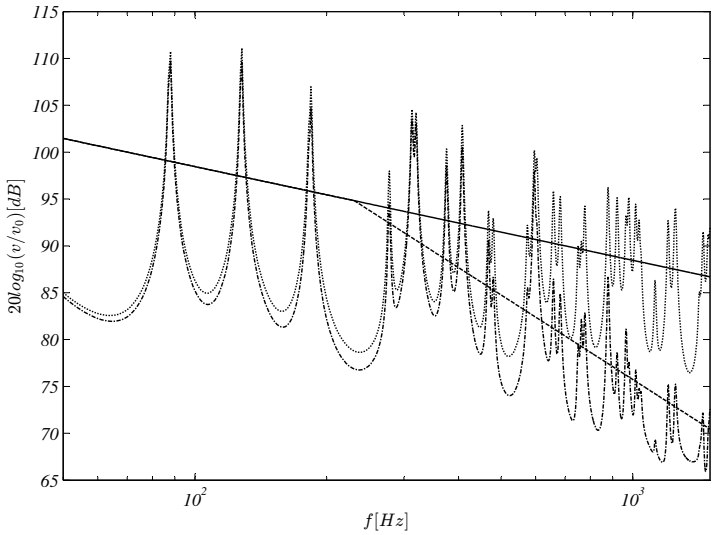

Figure 2.8: Numerical investigation compared to the proposed analytical model. Average square velocity of an aluminium plate with dimensions 1 m, 0.8 m and 0.005. Plate numerical (solid line) Eq. (2.20), plate analytical (dotted lines), associated patch-plate numerical (dotted-dashed line) and analytical (dashed line) Eq. (2.42).

patch-plate using

$$W_i = \rho_0 c_0 S \overline{v_i^2}\,\overline{\sigma_i}. \tag{2.48}$$

For $f < f_{Ns}$ the ratio between the sound power of the patch-plate and the actual plate, W_p/W, is unity since the patch-plate shows the same mean square velocity and average radiation efficiency compared to the actual plate. It is interesting to analyse the function W_p/W in the frequency range between f_{Ns} and f_{N0}. Thus, by combining Eqs. (2.20), (2.40), (2.46) the patch to plate power ratio is given by

$$\frac{W_p}{W} = \frac{256\overline{C^2}}{\pi^2 d^4 k_s^4} \frac{\mu_s\sqrt{\mu_s^2-1}}{\mu_p\sqrt{\mu_p^2-1}} \frac{ln\left(\frac{\mu_p+1}{\mu_p-1}\right)+\frac{2\mu_p}{\mu_p^2-1}}{ln\left(\frac{\mu_s+1}{\mu_s-1}\right)+\frac{2\mu_s}{\mu_s^2-1}}. \tag{2.49}$$

By writing the series expansion of the natural logarithm, $ln(x) = \sum_{n=1} \frac{1}{n}\left(\frac{x-1}{x}\right)^n$, which is valid for $x > 1/2$, Eq. (2.49) can be simplified in

$$\frac{W_p}{W} = \frac{256\overline{C^2}}{\pi^2 d^4 k_s^4} \frac{\mu_s\left(2\mu_p-1\right)}{\mu_p\left(2\mu_s-1\right)} \frac{\left(\mu_s^2-1\right)^{3/2}}{\left(\mu_p^2-1\right)^{3/2}}. \tag{2.50}$$

One may insert Eq. (2.43) and Eq. (2.44) in Eq. (2.50). For $f_{Ns} < f < f_{N0}$ one may note that $d \gg \lambda_s$ and $k_s \gg k_0$ therefore the following simplification can be introduced:

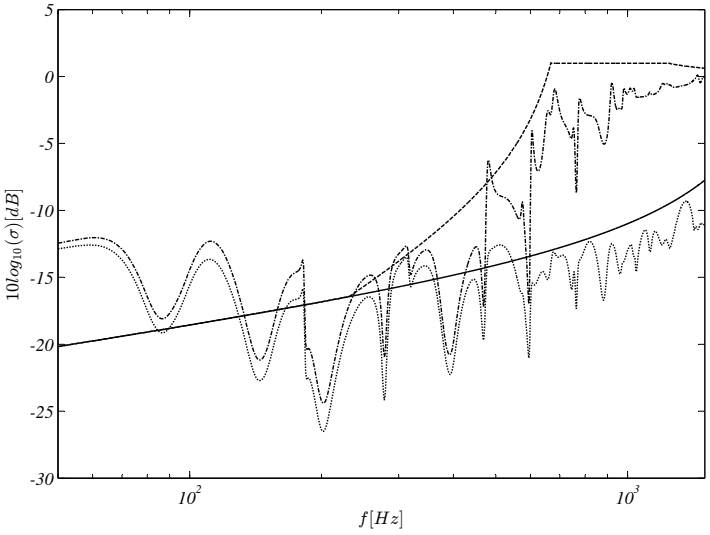

Figure 2.9: Comparison between numerical and analytical models. Radiation efficiency of an aluminium plate with dimensions 1 m, 0.8 m and a thickness of 0.005 m. Plate numerical (solid line), plate analytical (dotted lines) Eq. (2.46), associated patch-plate numerical (dotted-dashed line) and analytical (dashed line) Eqs. (2.45-2.47).

$k_0 d - 2k_s d \approx -2k_s d$ and $\left[\left(\frac{k_s d}{k_0 d}\right)^2 - 1\right] \approx \left(\frac{k_s d}{k_0 d}\right)^2$. Thus, in the mentioned frequency range Eq.(2.50) can be approximated by

$$\frac{W_p}{W}(\omega) = \frac{256\overline{C^2}}{\pi^2 k_p d} \frac{1}{-2d\sqrt[4]{\frac{\overline{m}}{D}}} \frac{\frac{d}{c_0}\omega - 2k_p d}{\sqrt{\omega}\left[(k_p d)^2 - \left(\frac{d}{c_0}\omega\right)^2\right]^{3/2}}. \tag{2.51}$$

One may define the first two terms in Eq. (2.51) as β, $\gamma = d/c_0$ and $\delta = k_p d = 2\pi/2.3$, therefore

$$\frac{W_p}{W}(\omega) = \beta \frac{\gamma\omega - 2\delta}{\left(\delta^2\omega^{1/3} - \gamma^2\omega^{7/3}\right)^{3/2}}. \tag{2.52}$$

The value of the function W_p/W at the minima gives an estimation of the maximum deviation in the assessment of the radiated power. Therefore one may asses the maxima and minima of Eq. (2.52) by setting its derivative equal to zero

$$\frac{d\left(\frac{W_p}{W}\right)}{d\omega} = \beta \frac{\gamma\left(\delta^2\omega^{1/3} - \gamma^2\omega^{7/3}\right) - \frac{1}{2}\left(\gamma\omega - 2\delta\right)\left(\delta^2\omega^{-2/3} - 7\gamma^2\omega^{4/3}\right)}{\left(\delta^2\omega^{1/3} - \gamma^2\omega^{7/3}\right)^{5/2}} = 0. \tag{2.53}$$

The maxima and minima of Eq. (2.52) are given by the roots of the following third order equation

$$\omega^3 - \frac{14}{5}\frac{\delta}{\gamma}\omega^2 + \frac{1}{5}\left(\frac{\delta}{\gamma}\right)^2\omega + \frac{2}{5}\left(\frac{\delta}{\gamma}\right)^3 = 0, \tag{2.54}$$

which can be solved by means of Cardano's formula. For $f_{Ns} < f < f_{N0}$ the minimum of Eq. (2.51) is given by

$$\omega_{min} = \left(\frac{56}{69} - \frac{A_1}{2} - \frac{A_2}{2} - \frac{B}{2}\right)\frac{\pi c_0}{d} \cong 1.250\frac{c_0}{d}, \tag{2.55}$$

where $A_1 = \sqrt[3]{c_1 + \sqrt{-c_2}}$, $A_2 = \sqrt[3]{c_1 - \sqrt{-c_2}}$, $B = j\sqrt{3}\,(A_1 - A_2)$, $c_1 \cong 0.342$ and $c_2 \cong 0.108$. By inserting Eq.(2.55) in Eq.(2.51) the maximum error results in

$$\frac{W_p}{W}(\omega_{min}) = \frac{2.680}{\sqrt{c_0 d\sqrt{\overline{m}/D}}} = \varepsilon. \tag{2.56}$$

Eq. (2.56) is a function of the material properties, thickness, sound speed of the fluid and the patch size. If one allows for a given error ϵ [dB] (e.g. $-1dB$) one may adopt a coarser discretisation

$$d_\epsilon = 1.143\frac{c_0}{10^{\epsilon/5} f_c}. \tag{2.57}$$

By inserting Eq. (2.57) in Eq. (2.51) and by plotting the function $W_p/W(\omega)$, it is possible to assess the frequency limit for which the patch-plate gives the same radiated power of the actual plate within $\pm\epsilon dB$ error, see Fig. 2.10. For instance, for $\pm 1dB$ error

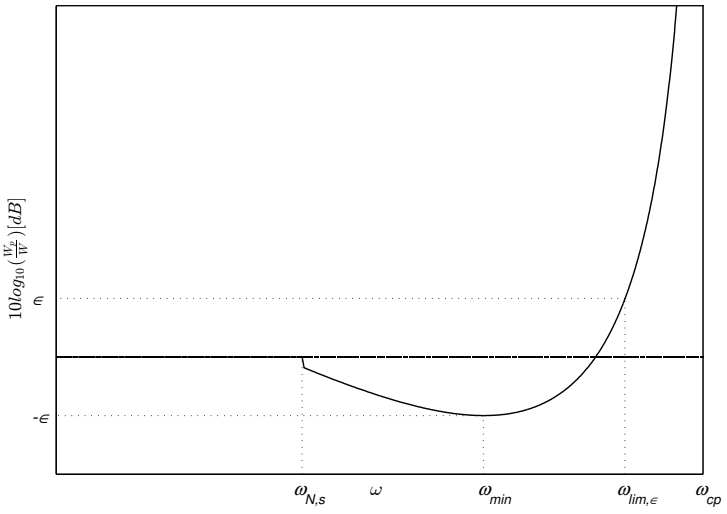

Figure 2.10: Power ratio, Eq. (2.51), as a function of the angular frequency below patch-plate coincidence.

in the power estimation for the plate specified in Table 2.1, one could use Eq. (2.57) to determine the corresponding discretisation. This results in a patch size of $0.25m$ rather than $0.16m$ which allows to reach a frequency limit of $442Hz$ compared to a structural Nyquist limit of $140Hz$. The patch-plate coincidence appears at $f = 583Hz$.

Fig. 2.11 shows the influence of the patch size on the power estimation error. The patch size is normalised with respect to the one based on the structural Nyquist criterion. Since the number of patches is inversely proportional to the square of the patch dimen-

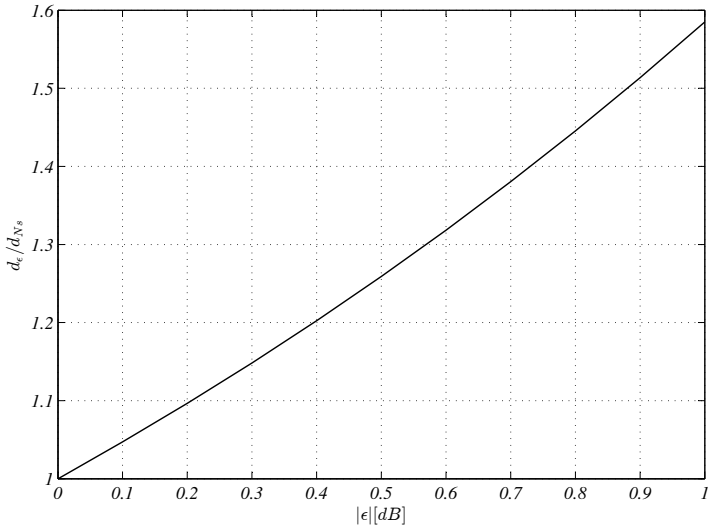

Figure 2.11: Increase of the patch dimension as a function of the maximum error allowed in the sound power estimation.

sion, a relatively small increase of the patch size may lead to a substantial reduction of the amount of patches.

The comparison between the analytically and numerically assessed power ratio is presented in Fig. 2.12, where the ratio $10log_{10}(W_p/W)$ for the plate which details are shown in Table 2.1. Based on the structural Nyquist sampling criterion the patch dimension would be $0.16m$. If one allows for $0.5dB$ error (10% error in [Watt]) on the power estimation a patch size of $0.2m$ can be chosen instead. This allows for a reduction of the experimental or numerical effort without deteriorate significantly the accuracy of the investigation. The analytical expressions Eqs. (2.20), (2.42) and (2.45-2.47) give an excellent agreement compared to the numerical results. Three different region can be identified. For frequencies lower that $230Hz$ both structural and acoustic Nyquist sampling criteria are satisfied. In this case the power radiated by the patch plate is equivalent to the one of the actual structure. In this frequency band the patch-plate is able to correctly describe the structural mode shapes of the plate. For $230Hz < f \leq 745Hz$ only the acoustic Nyquist sampling criterion is satisfied. The power radiated by the plate and the corresponding discretised system are approximately equal, an overestimation of $4.5dB$ is reached at the patch-plate coincidence ($f = 745Hz$). Finally, for

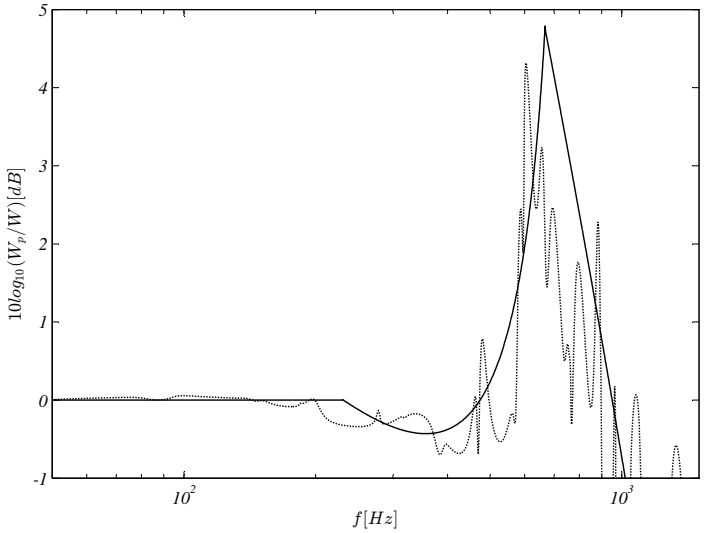

Figure 2.12: Comparison between the analytically (solid line) and numerically (dotted line) assessed power ratio.

$f > 745Hz$, both sampling criterion are not fulfilled and the acoustic power of the patch-plate diverges from the one of the actual plate. Above the patch-plate coincidence the averaging process still reduces the structural velocity but does not increases the radiation efficiency.

Chapter 3

A PTF-based characterisation of porous materials

3.1 Introduction

In many application fields, such as automotive and aerospace, the full FE Biot model has been widely applied to vibroacoustics problems involving poro-elastic materials in order to predict their structural and acoustic performance. The main drawback of this approach is however the large computational burden and the uncertainty of the input data (Biot parameters) that may lead to less accurate predictions. In order to overcome these disadvantages industry is asking for more efficient techniques. In this chapter a novel PTF based experimental technique for the characterisation of poro-elastic material is presented. The proposed procedure allows to perform the characterisation in conditions similar to the mounted situation. This feature is important since poro-elastic liners consist of solid and fluid phase that are excited with different efficiency depending on the boundary conditions. The experimental procedure is non-destructive and suitable for flat samples. Non-local effects due to in-plane wave propagation through the liner are accounted for by transfer terms. Propagation across the thickness of the material is described by cross terms.

3.2 Direct characterisation

To directly obtain the patch interface impedance matrix $\boldsymbol{Z}$ of the porous material we have to excite with a surface velocity v_j at a certain patch j and block all other patches so that $v_{k\neq j} = 0$. Then the impedance relation between patch i and the patch j is given by the ratio of averaged blocked surface pressure to the averaged surface velocity, see Eq. (1.5). Here, an example is given for a rectangular layer of Basotect TG melamine foam. In order to block the velocity at the interface steel plates with dimension $0.2m \times 0.2m \times 30mm$, and a weight of $9.5kg$ have been laid down on the sample. Due to the high mass and the high stiffness the rigid body modes of the plate on the sample, a melamine foam, appeared at very low frequencies while the first structural mode of the steel plate itself were at very high frequencies. All 6 mass-spring resonances of the plates on the foam specimen were located at frequencies equal or below $40Hz$ and the first structural resonance of the plates themselves above $2.4kHz$. The high impedance mismatch between the foam and the steel plates and the wide frequency range without any resonance allowed for a proper blocking condition between 100 Hz and 1.5 kHz. Thus the full frequency range of interest ($50Hz$ - $1kHz$) could be experimentally investigated. Therefore a patch size of $0.2m$ times $0.2m$ has been chosen for the experimental characterisation of the specimen. An up-scaling to a bigger size multiple of 0.2 m can be easily perform in the post-processing phase by means of the superposition principle. The results that will be shown in the following section are referred to $0.4m \times 0.4m$ square patches. Since the blocking steel plates show no modes inside the investigated frequency range a uniform velocity excitation over the patch could be obtained by simply hammer excitation in the centre of a steel plate. The imposed velocity on the excited patch has been measured by an accelerometer attached close by the centre of the steel plate. The plates must not be in contact with each other and at the same time the gap between the plates shall be kept as small as possible in order to avoid energy leaks through the slits. The interface pressure has been measured by 4 1/4 inch pressure microphones embedded into each steel plate flush to the foam interface. Note that by doing so only the pressure contribution due to the interstitial fluid is accounted for, whereas the pressure contribution of the skeleton is neglected. The experimental characterisation of the porous material has been carried out on a melamine sample of $0.8m \times 0.4m \times 42mm$ thick fully blocked by the steel plates on the top, the blocking conditions on the bottom surface have been provided by a rigid reinforced concrete floor. The setup is shown in Fig. 3.1.

3.2.1 Numerical validation

The experimental methodology for the characterisation of porous materials has been validated by means of a equivalent fluid model integrated into an FE numerical model. In case that the skeleton motion can be neglected the porous material can be replaced by an equivalent fluid domain with a complex density and a complex bulk modulus. The assessment of these complex quantities can be achieved by means of empirical models such as the one proposed by Delany and Bazley [11], [20]. If the porous material has a high porosity the complex wavenumber k and the characteristic impedance Z_c can

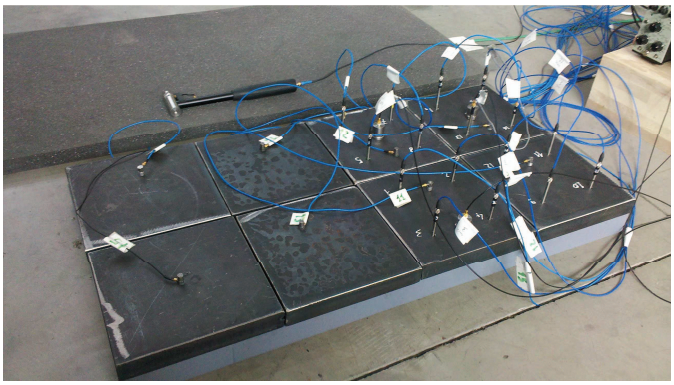

Figure 3.1: Set-up for the experimental direct characterisation of a poroelastic liner.

be calculated from the flow resistivity σ as a function of the frequency f and the fluid properties ρ_0 and c_0

$$Z_c = \rho_0 c_0 \left[1 + 0.0057 \left(\frac{\rho_0 f}{\sigma}\right)^{-0.754} - j0.087 \left(\frac{\rho_0 f}{\sigma}\right)^{-0.732}\right] \tag{3.1}$$

$$k = \frac{2\pi f}{c_0} \left[1 + 0.0978 \left(\frac{\rho_0 f}{\sigma}\right)^{-0.700} - j0.189 \left(\frac{\rho_0 f}{\sigma}\right)^{-0.595}\right] \tag{3.2}$$

with the following validity range

$$0.01 \leq \frac{\rho_0 f}{\sigma} \leq 1 \tag{3.3}$$

The FE validation has been carried out by numerical modelling which mimics the experimental procedure. The FE model of the melamine foam consisted of an equivalent fluid with rigid boundary conditions applied on the bottom surface. An imposed velocity has been applied on the excited patch while the other patches have been blocked. In order to assess the impedance matrix of the full sample this procedure must be repeated for all the patches. The response over each patch has been obtained by integrating the pressure over the patch surface. The input parameters for the numerical model are the speed of sound and the density of air, $343m/s$ and $1.2kg/m^3$ respectively, and the foam flow resistivity of 11350 Ns/m4. These parameters have been measured on a sample of the same batch of the material as used during the presented work. For the given flow resistivity the Delany and Bazley model is valid from $95Hz$ to $9.5kHz$. In the calculation the vertical edges of the equivalent fluid have been blocked. The characterisation has been carried out on two $0.4m \times 0.4m$ patches located in the centre of a specimen of dimensions $1.7m \times 0.8m \times 0.042m$. Therefore continuity type of boundary condition are applied at the vertical edges of the two patches. In Fig. 3.2 the impedance relations between two patches are defined. If port 1 is excited by a uniform velocity the input impedance Z_{in} is defined as the pressure response due to a velocity excitation applied on

the same port. The transfer impedance Z_{tr} is the pressure response on port 2. Results

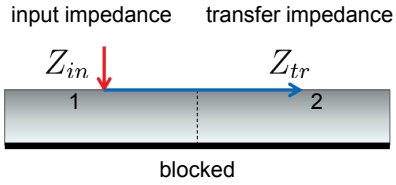

Figure 3.2: Definition of the impedance terms between two patches for a single-layered liner.

of the experimental characterisation compared to the numerical validation are shown in Fig. 3.3, where the impedance level ($L = 10logZ$) and phase are plotted as a function of the frequency. Although strictly speaking the Delany and Bazley model was developed

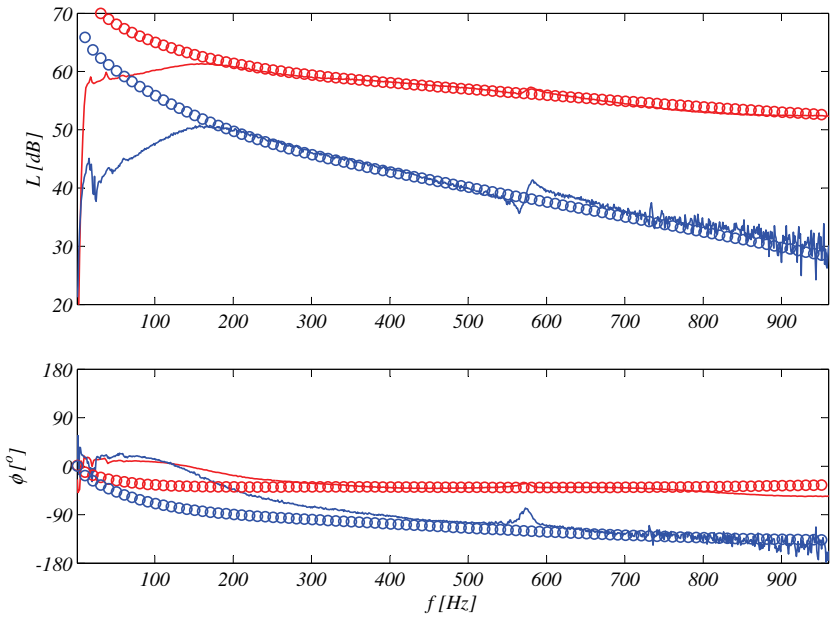

Figure 3.3: Direct characterisation method of melamine foam with $0.4m$ patches: input patch impedance Z_{in} (red), transfer patch impedance Z_{tr} (blue), experiment (solid lines), numerical (o markers).

for fibre based materials, an excellent agreement can be observed starting from $200Hz$ onwards. Low frequency deviations could not be ascribed to Delany and Bazley inaccuracies (the Miki correction, for instance, did not influence the low frequency signature) but turned out to depend on the boundary conditions at the vertical edges, as will be discussed below.

A second model has been realised in order to investigate the effects of the boundary conditions applied to the vertical edges of the patches. We can distinguish between two limit cases: blocked edges and free edges. These two different conditions have been investigated by means of numerical models in which the specimen has dimension of $0.8m \times 0.4m$. In this case the vertical edges of the specimen are blocked (blocked edges) or radiating into a semi-infinite space (free edges). Perfectly Matched Layer boundary conditions are used in order to avoid reflections at the outer boundary of the fluid mesh. The outcome is shown in Fig. 3.4. The boundary conditions imposed at the vertical edges of the sample strongly influence the patch impedance below $200Hz$. When the vertical

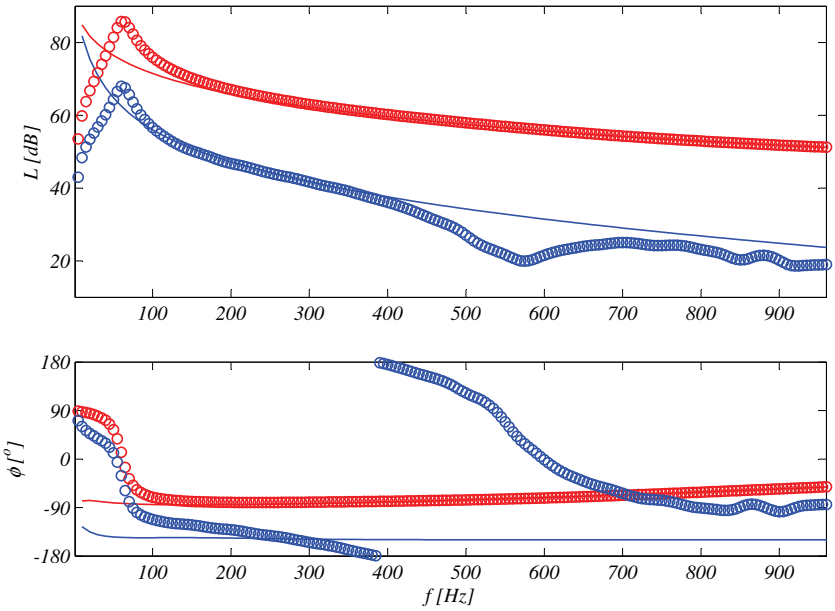

Figure 3.4: Effects of boundary condition imposed at the vertical edges of the sample on the foam patch impedance; input patch impedance Z_{in} (red), transfer patch impedance Z_{tr} (blue). (i) blocked edges (solid lines); (ii) free edges (o markers).

edges are blocked the impedance amplitude is inversely proportional to the frequency and the phase starts at -90 degrees. This trend can be interpreted as stiffness behaviour. In the case the edges are free the impedance amplitude is directly proportional to the frequency in the low frequency range and the phase has a value of $+90$ degrees. This behaviour represents mass governed edge radiation impedance through the edges of the foam into air. If the patches are defined far away from the sides of the specimen, the edges of the patches are radiating into foam: continuity type of boundary conditions are imposed at the edges of the patches. The boundary conditions imposed on the vertical edges of the liner during the experimental characterisation are however different from

the three cases described above, since it was difficult in the experiment to reproduce well defined boundary conditions precisely (blocked edges). Since the effects of the boundary conditions imposed at the vertical edges of the foam strongly influence the low frequency behaviour of the trim, it is important to execute the sound package characterisation with the same boundary conditions that will be imposed to the liner on the assembled system.

3.3 Indirect characterisation

The practical applicability of the direct procedure for the characterisation of industrial types of sound insulation systems turned out to be rather limited. For this reason the indirect characterisation technique based on the solution of an inverse problem has been proposed as an alternative method to assess the trim impedances. The patch impedance matrix of lining materials can be also derived in an indirect manner, in which blocking conditions are not satisfied at the specimen interface during the test. In this case, both pressure and velocity have to be determined at the interface. In order for Z to be obtained on N patches, one needs to create N linear independent load conditions, which correspond to N different p and v configurations. The PTFs impedances are then reconstructed by solving the associated inverse problem

$$\mathbf{Z} = \mathbf{P}\mathbf{V}^{-1}. \tag{3.4}$$

The indirect trim characterisation approach resembles the direct method, in which the trim specimen is laid down on a rigid surface and its upper interface is excited and measured from the open top. The excitation is provided by loudspeakers located above the trim, whereas the fluid pressure and normal velocity are directly measured by a Microflown PU probe array in the vicinity of the trim-fluid interface. The set-up is shown in Fig. 3.5. This technique allows for the assessment of the surface input and

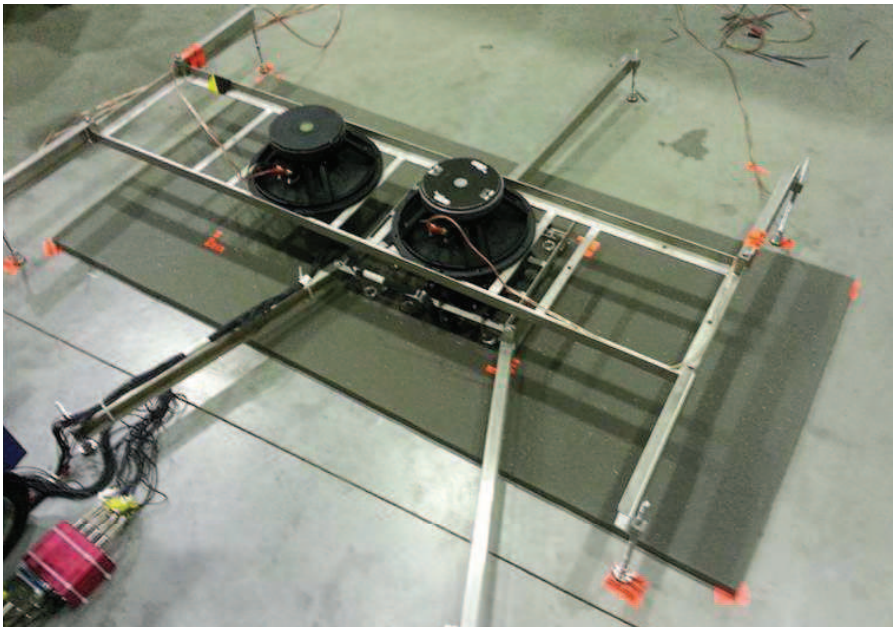

Figure 3.5: Set-up for the indirect experimental characterisation of a poroelastic liner.

surface transfer impedance on the open top interface of the specimen and is therefore not suited for the assessment of the cross impedance relations between the patches placed on two opposite faces of the specimen. In order to capture the non local behaviour of

the material the transverse wave propagation must be taken into account. This leads to a set-up made of two (or more) adjacent patches. The relation between the pressure and velocity in case of n patches reads

$$\begin{pmatrix} v_1 \\ v_2 \\ \vdots \\ v_n \end{pmatrix} \begin{pmatrix} z_{11} & z_{12} & \dots & z_{1n} \\ z_{21} & z_{22} & \dots & z_{2n} \\ \vdots & \vdots & \ddots & \vdots \\ z_{n1} & z_{n2} & \dots & z_{nn} \end{pmatrix} = \begin{pmatrix} p_1 \\ p_2 \\ \vdots \\ p_n \end{pmatrix}. \tag{3.5}$$

If the trim material is highly damped one may consider only the input impedance and the transfer to the next neighbour. Since the procedure consists in the characterisation of two patches, two linearly independent load cases have to be established in order for the equation system to be well posed. The matrix Eq. (3.5) can be rewritten as follows

$$\begin{pmatrix} v_1' & v_1'' \\ v_2' & v_2'' \end{pmatrix} \begin{pmatrix} z_{11} & z_{12} \\ z_{21} & z_{22} \end{pmatrix} = \begin{pmatrix} p_1' & p_1'' \\ p_2' & p_2'' \end{pmatrix}. \tag{3.6}$$

In order to solve the Eq. (3.6) for the sought impedance, the pressure matrix is multiplied by the inverted velocity matrix

$$\begin{pmatrix} z_{11} & z_{12} \\ z_{21} & z_{22} \end{pmatrix} = \begin{pmatrix} p_1' & p_1'' \\ p_2' & p_2'' \end{pmatrix} \begin{pmatrix} v_1' & v_1'' \\ v_2' & v_2'' \end{pmatrix}^{-1}, \tag{3.7}$$

which yields the patch blocked surface input $Z_{in} = Z_{11} = Z_{22}$ and transfer $Z_{tr} = Z_{12} = Z_{21}$ impedances of the specimen. The results are presented in Fig. 3.6 in terms of impedance level and phase. A good agreement between experimental and numerical results can be observed. The indirect approach is characterised by higher noise levels compared to the direct method. As expected the transfer impedance is affected by a higher noise compared to the input one. The high energy losses in the transverse wave propagation phenomena determines a lower signal in the neighbouring patch. The low frequency range, where the effects of boundary conditions applied on the vertical edges of the liner become important, is affected by a high noise level.

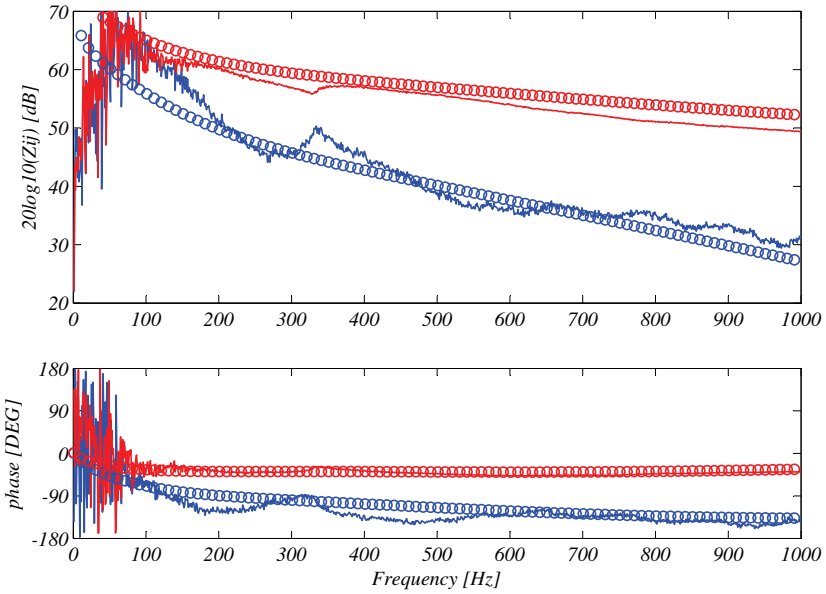

Figure 3.6: Indirect characterisation method of melamine foam with $0.4m$ patches: input patch impedance Z_{in} (red), transfer patch impedance Z_{tr} (blue), experiment (solid lines), numerical (o markers).

3.4 Air layer correction

For technical reasons the PU sensors are not measuring at the real interface between the specimen and the surrounding fluid. Therefore, by means of the indirect technique the impedance of the material in series with a tiny layer of air is determined. By writing the continuity conditions at the interface of each layer it is possible to determine the relation between the measured impedance Z_m and the actual impedance of the material Z_t and the air slit Z_a, see Fig. 3.7. The continuity conditions for pressure at the interfaces 1, 2

Figure 3.7: Two layers of different properties connected in series.

and 3 are respectively

$$\begin{aligned} p_1 &= Z_a v_1 - Z_a v_2 \\ Z_a v_1 - Z_a v_2 &= -Z_{22} v_2 - Z_{23} v_3 \\ Z_{t,32} v_2 + Z_{t,33} v_2 &= p_3. \end{aligned}$$

This linear system can be re-written in a matrix form

$$\begin{pmatrix} Z_a & -Z_a & 0 \\ Z_a & -Z_a - Z_{t,22} & -Z_{t,23} \\ 0 & Z_{t,32} & Z_{t,33} \end{pmatrix} \begin{pmatrix} v_1 \\ v_2 \\ v_3 \end{pmatrix} = \begin{pmatrix} p_1 \\ p_2 \\ p_3 \end{pmatrix}. \tag{3.8}$$

Solving by substitution leads to

$$\begin{pmatrix} p_1 \\ p_3 \end{pmatrix} \begin{pmatrix} \frac{Z_{t,22} Z_a}{Z_{t,22} - Z_a} & \frac{Z_{t,23} Z_a}{Z_{t,22} - Z_a} \\ -\frac{Z_{t,32} Z_a}{Z_{t,22} - Z_a} & \frac{-Z_{t,23} Z_{t,32} + Z_{t,22} Z_{t,33} - Z_a Z_{t,33}}{Z_{t,22} - Z_a} \end{pmatrix} = \begin{pmatrix} v_1 \\ v_3 \end{pmatrix}, \tag{3.9}$$

that is equivalent to the measured impedance

$$\begin{pmatrix} p_1 \\ p_3 \end{pmatrix} \begin{pmatrix} Z_{m,11} & Z_{m,13} \\ Z_{m,31} & Z_{m,33} \end{pmatrix} = \begin{pmatrix} v_1 \\ v_3 \end{pmatrix}. \tag{3.10}$$

Finally, by comparing Eq. (3.9) and (3.10) it is possible to determine the relations between measured and specimen impedances

$$Z_{t,22} = \frac{Z_{m,11} Za}{Z_{m,11} - Za} \tag{3.11}$$

$$Z_{t,23} = \frac{Z_{m,13}Za}{Z_{m,11} - Za} \tag{3.12}$$

$$Z_{t,32} = -\frac{Z_{m,31}Za}{Z_{m,11} - Za} \tag{3.13}$$

$$Z_{t,33} = Z_{m,33} - \frac{Z_{m,13}Z_{m,31}}{Z_{m,11} - Za}. \tag{3.14}$$

By rewriting Eq. 3.11 as follow

$$Z_{t,22} = \frac{Z_{m,11}}{\frac{Z_{m,11}}{Za} - 1}, \tag{3.15}$$

one may note that the effect of the air slit becomes negligible if the impedance of the air slit is much higher than the impedance of the specimen, as in the case of the melamine foam. The air gap correction is not negligible if the air slit impedance is of the same order of magnitude or much lower compared to the material sample impedance. In order to asses the actual impedance of the liner the air slit has to be characterised.

3.4.1 Air layer impedance characterisation

If the air layer between the measurement plane of the PU probe array and the interface of the material is small compared to the wavelength, the fluid pressure can be considered constant across the air gap thickness. Under this assumptions, one may asses the impedance of the media confined between the lower blocking surface and the actual measurement plane just by measuring fluid pressure and velocity. An example of air slit impedance is shown in Fig. 3.8. By observing the input impedance we may recognise a mass-spring type of behaviour. The stiffness is given by the air layer thickness while the mass behaviour is determined by the mass governed radiation through the vertical edges. In Fig. 3.9 the effect of the air slit correction on the characterisation of a $16mm$ layer of polyurethane (PU) foam is shown. The correction especially affects the low frequency range where the cross-talking through the air layer between two neighbouring patches is important.

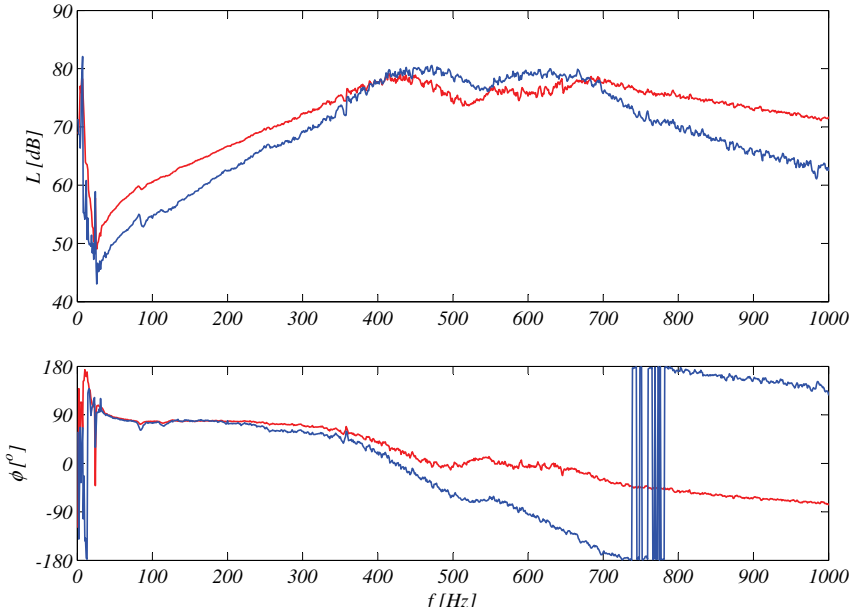

Figure 3.8: Air layer input Z_{in}(red) and transfer Z_{tr} (blue) surface impedance.

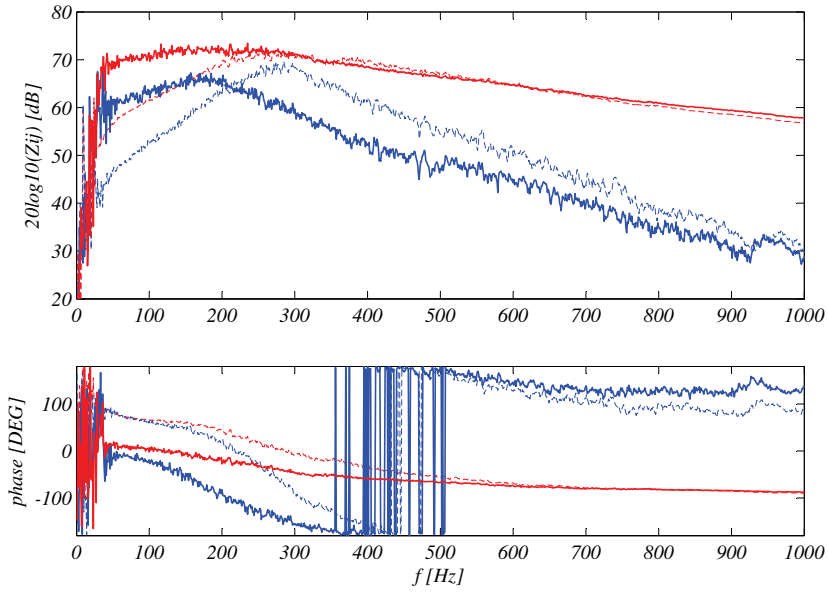

Figure 3.9: Characterisation of a PU foam layer: comparison between uncorrected (dashed) and corrected (solid) input Z_{in} (red) and transfer Z_{tr} (blue) surface impedance.

3.5 Characterisation of multilayer materials

Acoustic treatments made of multilayer materials are often used in automotive and building acoustic applications. Usually, porous materials for acoustic applications are characterised by high porosity such that the solid phase occupies less than 5% of the total volume. Moreover, a septum can be glued on top of the porous layer in order to achieve a mass-spring damping system. The coupling of such liners with a structure introduces damping, additional mass and it decouples the structure from the cavity. Furthermore, absorption is added in the acoustic domain.

The proposed characterisation procedure consists in a non destructive test where the liner is considered as a black box. Therefore, the specimen is characterised as an all, without the need for the identification of the mechanical and vibro-acoutic properties of each layer. In this work flat specimen with layers of constant thickness are considered, hence the macroscopic characteristics of the liners can be considered uniform over the surface and along the thickness. Therefore simplifications may be introduced in case of geometrical symmetries.

The purpose of the approach is the assessment of surface impedance relations (PTFs) at both specimen faces in terms of patches. This also accounts for the wave propagation across the thickness of the liner. In order to take the transverse wave propagation into account the set-up design requires at least a 2 patch layout. This is essential in order to take into account the non-local behaviour of the material.

A key objective is the characterisation of a specimen facing representative excitation and boundary conditions compared to operational conditions. Typically, a poro-elastic layer is attached on a master structure and it is coupled with an acoustic domain. At the structure-porous interface both skeleton and fluid phase are excited efficiently since stress concentration occurs in the contact areas between skeleton and structure. As a consequence solid and fluid phase will show the same velocity. In order to recreate these features in the test set-up the specimen is laid down on a mechanical piston. This allows for efficient excitation of both phases of the porous material. Moreover, in order to measure the fluid and solid phase reaction, both average pressure and velocity are determined in an indirect way by reading the piston reaction force and acceleration. At the fluid-porous interface only the fluid phase is excited efficiently. This is due to the fact that the fluid cannot withstand shear stresses. Therefore, stress concentrations cannot occur and the excitation of the skeleton can be considered as negligible. The fluid phase dominates the problem so that the fluid pressure and the particle velocity reaction of the liner can be directly measured via pu-probes. Because of different type of excitation and boundary conditions, the specimen impedance matrix is not necessary symmetric. In order to assess the matrix $\boldsymbol{Z}$ containing all the surface impedance relations (PTFs) between N_p patches a set of $2N_p$ independent equations is needed. Thus, one needs to realize $2N_p$ independent load cases by combining shaker and loudspeaker excitation and to measure the average patch pressure and velocity at both interfaces. In principle, each patch should be equipped with a shaker on one side and a loudspeaker on the opposite side.

In case of symmetries the set-up can be simplified in order to reduce the measurement effort. If the material under testing is characterised by high damping and if a patch dimension of $0.2m$ is considered, the energy decays rapidly such that only the driven patch and the next neighbour have to be measured. If the macroscopic material properties can be considered homogeneous in the transverse directions then two symmetry axes can be introduced. Therefore the transfer impedance to the next patch is equal in all directions. This consideration allows to simplify the problem to a test bench made of 2 patches. In this case, a set of linear independent load cases is represented by the following four conditions:

i) shaker off, loudspeakers on and in phase;

ii) shaker off, loudspeakers on and in antiphase;

iii) loudspeakers off, shaker 1 on and shaker 2 off;

iv) loudspeakers off, shaker 1 off and shaker 2 on.

Furthermore, in this configuration only one active piston is necessary. The following three conditions are sufficient to create a complete set of independent load cases:

i) shaker off, loudspeaker on and in phase;

ii) shaker off, loudspeaker on and in antiphase;

iii) shaker on, loudspeakers off;

A fourth condition can be virtually created by copying and swapping the elements of the third column to the fourth column of the pressure and velocity matrices. Therefore, a passive piston can be installed. Since we are considering a quasi locally reacting material the reconstructed blocked impedance matrix of the specimen is a sparse banded matrix.

3.5.1 Experimental set-up

The experimental procedure consists first, in a calibration measurement without specimen and second, in the actual measurement with the sample laid down on the test bench. This has to be repeated $2N_p$ times: one time only the shaker is driven, then only the loudspeaker is excited. The lower and upper interface of the material sample are named a, b respectively, for each patch the average pressure and velocity response has to be measured at both interfaces p_i^a, v_i^a, p_i^b, v_i^b, see Fig. 3.10. A loudspeaker provides the acoustic excitation on the liner top interface. Sound pressure and particle velocity are directly measured by means of a Microflown pu-probe array. The patch average fields on each patch p_i^b, v_i^b are determined by averaging over the array sensors. At the bottom interface an electro-dynamic shaker provides mechanical excitation through a piston. The reaction pressure $p_{i,meas}^a$ and velocity v_i^a of the specimen are measured via force transducers and accelerometer respectively. A sketch of the set-up is shown in Fig. 3.11. If N_k force transducers are mounted between the shaker mounting plate and the

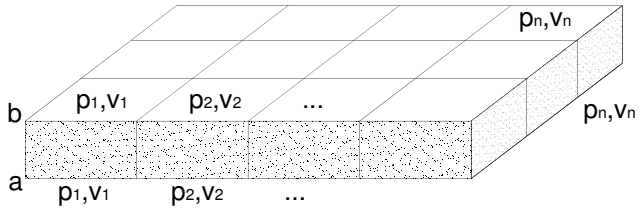

Figure 3.10: Sketch of a specimen sample: a and b are the top and bottom interface respectively.

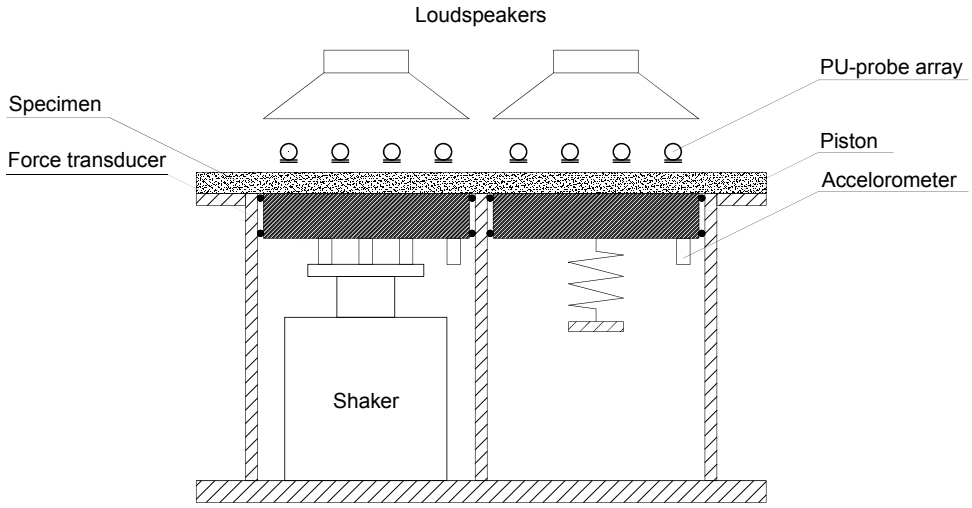

Figure 3.11: Sketch of the experimental set-up.

piston the measured pressure is defined as

$$p^a_{i,meas} = \frac{1/N_k \sum_{k=1}^{N_k} F_k}{dS}, \tag{3.16}$$

where F_k are the force signals and dS is the piston surface. The piston dimension matches the patch size and its mass is minimised in order to assure an acceptable dynamic range for the indirect pressure measurement. Furthermore, its stiffness is optimised in order to move the influence of the piston structural modes outside the frequency range of interest. The reaction pressure of the specimen is given by

$$p^a_i = p^a_{i,meas} - Z_{i,piston} v^a_i, \tag{3.17}$$

where $Z_{i,piston}$ is the impedance of the active piston determined by its mass and the fluid loading acting on the its free surface. The assessment of the piston impedance is

carried out without specimen, by matching pressure reading of the piston $F^a_{i,cal}/dS$ with pressure and velocity from the pu-probe array $p^a_{i,cal}$, $v^a_{i,cal}$. Only the shaker is driven and the pu-probe array is installed as close as possible to the piston top surface. The impedance of the passive piston is given by

$$Z_{i,piston} = \frac{1}{v_{i,cal}} \left(\frac{F^a_{i,cal}}{dS} - p^a_{i,cal} \right). \tag{3.18}$$

The calibration of a passive piston is again carried out without specimen and by driving only the loudspeaker. The pu-probe array is positioned above the piston surface in order to measure directly sound pressure $p^a_{j,cal}$ and particle velocity $v^a_{j,cal}$. The piston impedance is

$$Z_{j,piston} = \frac{p^a_{j,cal}}{v^a_{j,cal}}, \tag{3.19}$$

where $Z_{j,piston}$ takes into account the piston mass and the fluid loading acting on the its free surface. Therefore the reaction pressure of the specimen can be assess indirectly by

$$p^a_{j,cal} = Z_{j,piston} v^a_j, \tag{3.20}$$

where v^a_j is the velocity of the passive piston measured by an accelerometer.

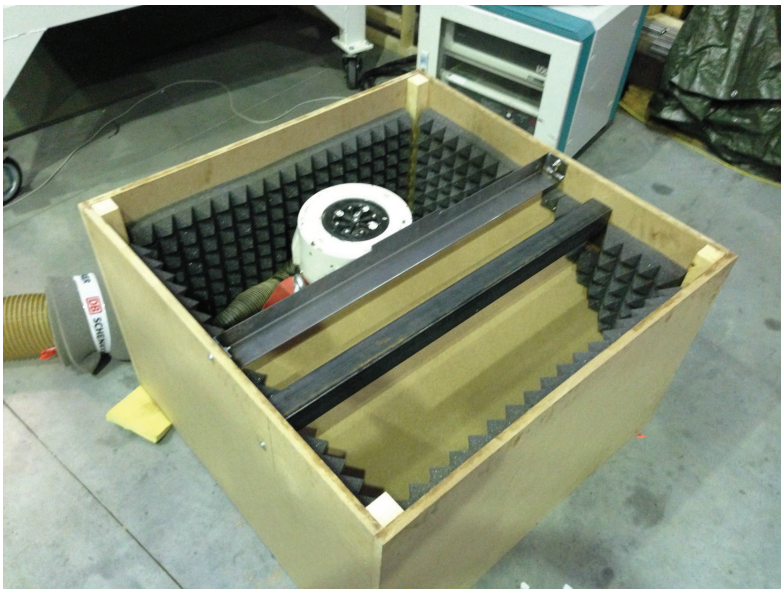

Figure 3.12: Picture of the experimental set-up: the shaker and the mounting beams for he passive piston are visible.

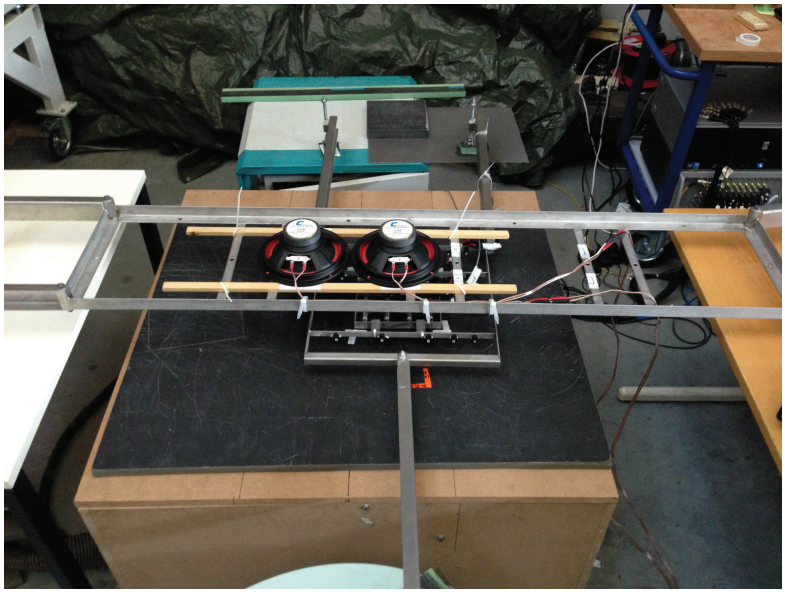

Figure 3.13: Picture of the experimental set-up: trim test rig during liner characterisation.

3.5.2 Specimen impedance assessment

In order to determine the blocked impedance matrix of the material the following system of linear equations has to be solved

$$\mathbf{Z} = \mathbf{P}\mathbf{V}^{-1}. \tag{3.21}$$

Eq. (3.21) can be written as

$$\begin{aligned}\mathbf{Z} = &\left(\begin{bmatrix} \mathbf{p}^a \\ \mathbf{p}^b \end{bmatrix}^{i} \begin{bmatrix} \mathbf{p}^a \\ \mathbf{p}^b \end{bmatrix}^{ii} \cdots \begin{bmatrix} \mathbf{p}^a \\ \mathbf{p}^b \end{bmatrix}^{2N_p} \right) \\ &\left(\begin{bmatrix} \mathbf{v}^a \\ \mathbf{v}^b \end{bmatrix}^{i} \begin{bmatrix} \mathbf{v}^a \\ \mathbf{v}^b \end{bmatrix}^{ii} \cdots \begin{bmatrix} \mathbf{v}^a \\ \mathbf{v}^b \end{bmatrix}^{2N_p} \right)^{-1}.\end{aligned} \tag{3.22}$$

If only two patches are considered Eq.(3.22) reduces to

$$\begin{aligned}\begin{pmatrix} \mathbf{Z}_a & \mathbf{Z}_{ab} \\ \mathbf{Z}_{ba} & \mathbf{Z}_b \end{pmatrix} = &\left(\begin{bmatrix} \mathbf{p}^a \\ \mathbf{p}^b \end{bmatrix}^{i} \begin{bmatrix} \mathbf{p}^a \\ \mathbf{p}^b \end{bmatrix}^{ii} \begin{bmatrix} \mathbf{p}^a \\ \mathbf{p}^b \end{bmatrix}^{iii} \begin{bmatrix} \mathbf{p}^a \\ \mathbf{p}^b \end{bmatrix}^{iv} \right) \\ &\left(\begin{bmatrix} \mathbf{v}^a \\ \mathbf{v}^b \end{bmatrix}^{i} \begin{bmatrix} \mathbf{v}^a \\ \mathbf{v}^b \end{bmatrix}^{ii} \begin{bmatrix} \mathbf{p}^a \\ \mathbf{p}^b \end{bmatrix}^{iii} \begin{bmatrix} \mathbf{v}^a \\ \mathbf{v}^b \end{bmatrix}^{iv} \right)^{-1}.\end{aligned} \tag{3.23}$$

The vectors $\mathbf{v}$ and $\mathbf{p}$ represent the velocity excitation and pressure response at the respective interfaces a and b, for each load case $(i - iv)$. The vectors $\boldsymbol{Z^{aa}}$, $\boldsymbol{Z^{ab}}$, $\boldsymbol{Z^{ba}}$ and $\boldsymbol{Z^{bb}}$ contain the input, transfer and cross surface impedances of the liner. In order to create a well posed problem a orthogonal set of linear equations is needed. A bad conditioning can lead to an amplification of the measurement errors inherent in the experimental data. In principle, in order to minimise the conditioning in the inverse problem one may look for a set of orthonormal load cases.

The measurements at the upper interface of the material (a) have to be corrected for the air gap. The accuracy of the correction is affected by the high particle velocity gradient close to a hard surface. Therefore the PU probe array has to be precisely positioned such that the distance between the specimen and the sensors is constant during the all measurement procedures. The specimen could also be characterised with a defined air layer at the top surface. In this case the air gap is included in the characterisation and no correction would be necessary. Nevertheless, in this case further transfer terms would have to be characterised in order to take into account for propagation inside the air gap to more distant patches.

3.5.3 Characterisation results

Two liners have been characterised by means ot the trim test rig. First, a mass-spring system consisting of a $14mm$ PU foam layer with a density of $69kg/m^3$ and a $3kg/m^2$ heavy layer, here referred as mass-spring system 1. Second, a mass-spring system composed by a $14mm$ PU foam layer with a density of $85kg/m^3$ and a $2.2kg/m^2$ heavy layer of $3mm$ thickness on which a felt carpet is glued on top of it. This liner variant is referred as mass-spring system 2. In Fig. 3.14 the impedance relations between two patches are defined. If port 1 is excited by a uniform velocity the input impedance Z_{in}^{bb} is defined as the pressure response due to a velocity excitation applied on the same port. The transfer impedance Z_{tr}^{bb} is the pressure response on port 2. The cross impedance Z_{in}^{ba} is the pressure response on port 3. The cross-transfer impedance Z_{tr}^{ba} is the pressure response on port 4.

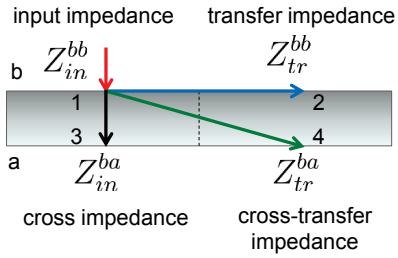

Figure 3.14: Definition of the impedance terms between two patches for a multi-layered liner.

Mass-spring system 1

The top surface input and transfer impedance, Z_{in}^{bb} and Z_{tr}^{bb} respectively, are shown in Fig. 3.15. By observing the input impedance one can recognise a mass-spring behaviour with a resonance at about $300Hz$. The liner impedance is dominated by the stiffness of the foam below the resonance and by the mass of the heavy layer above the resonance. Below $150Hz$ the effect of mass governed radiation impedance of the vertical edges is visible. Some measurement errors can be recognised below $150Hz$ and at $550Hz$ since the phase of the input impedance exceeds $\pm 90deg$. The top to bottom face cross and cross-transfer impedance, Z_{in}^{ba} and Z_{tr}^{ba} respectively, are shown in Fig. 3.16. The bottom to top face cross and cross-transfer impedance, Z_{in}^{ab} and Z_{tr}^{ab} respectively, are shown in Fig. 3.17. The comparison between the cross and cross-transfer terms of figure 3.16 and 3.17 shows that the cross terms are approximately reciprocal while the cross-transfer terms are not. For $f > 550Hz$ the phase of the cross impedance goes over $-90deg$, this can be an indication of the onset of the propagation of longitudinal waves across the thickness of the liner. Finally, the bottom to top cross-transfer impedance is characterised by a high noise level, especially above the mass-spring resonance frequency where the heavy layer is decoupled from the foam. The bottom surface input and transfer impedance, Z_{in}^{aa} and

Z_{tr}^{aa} respectively, are shown in Fig. 3.18. Below $50Hz$ the stiffness of the whole system due to the excitation of a single patch and blocking of the remaining patches is visible in the input impedance. Below $150Hz$ the effect of mass governed radiation impedance of the vertical edges is visible. For $150Hz < f > 500Hz$ the liner impedance is dominated by the stiffness of the foam. At higher frequencies a constant amplitude and a $0deg$ phase indicates that the propagating wave is damped across the thickness of the liner and no energy is reflected back. The transfer and cross-transfer terms are important in the low frequency range, below the mass-spring resonance of the liner. At higher frequencies the input and cross terms are $5dB$ to $10dB$ higher than the transfer and cross-transfer respectively. At frequencies below $100Hz$ the transfer and cross-transfer impedances are not reliable due to structural modes of the test rig and signal to noise problems.

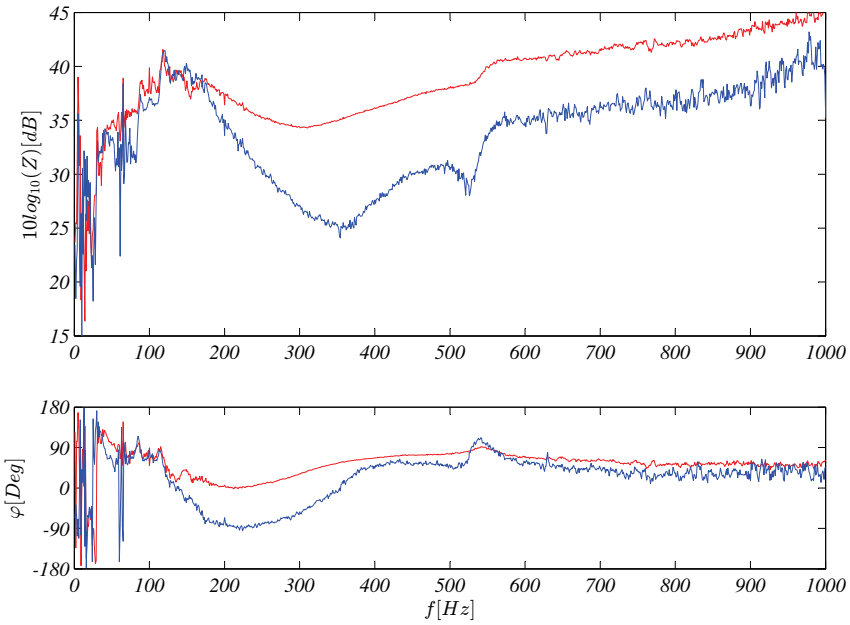

Figure 3.15: Top side surface input Z_{in}^{bb} (red) and transfer impedance Z_{tr}^{bb} (blue).

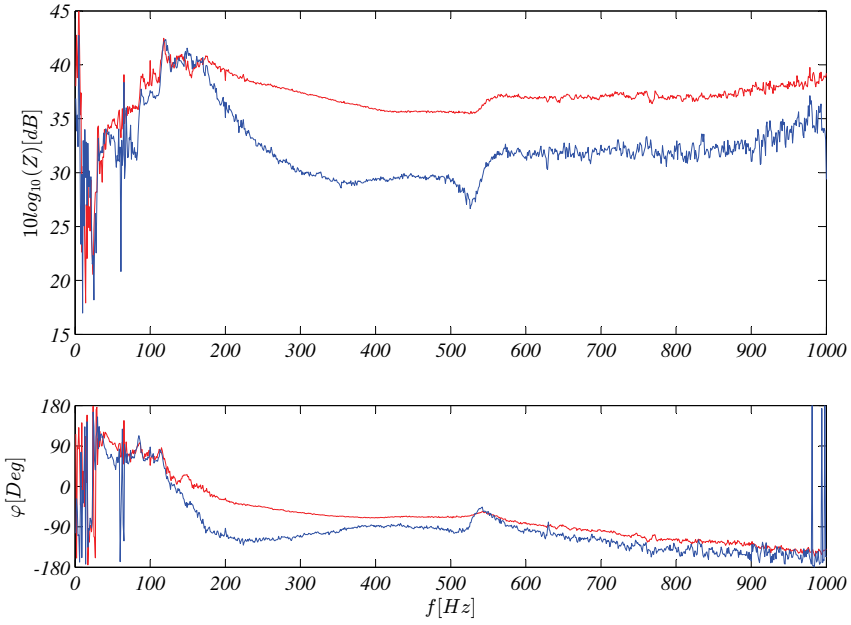

Figure 3.16: Top to bottom cross input Z_{in}^{ba} (red) and transfer impedance Z_{tr}^{ba} (blue).

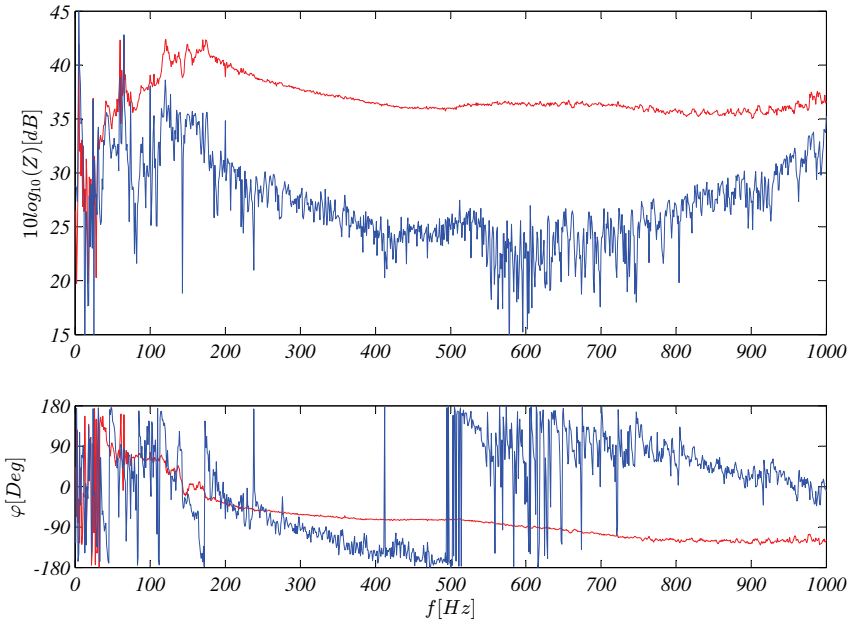

Figure 3.17: Bottom to top cross input Z_{in}^{ab} (red) and transfer impedance Z_{tr}^{ab} (blue).

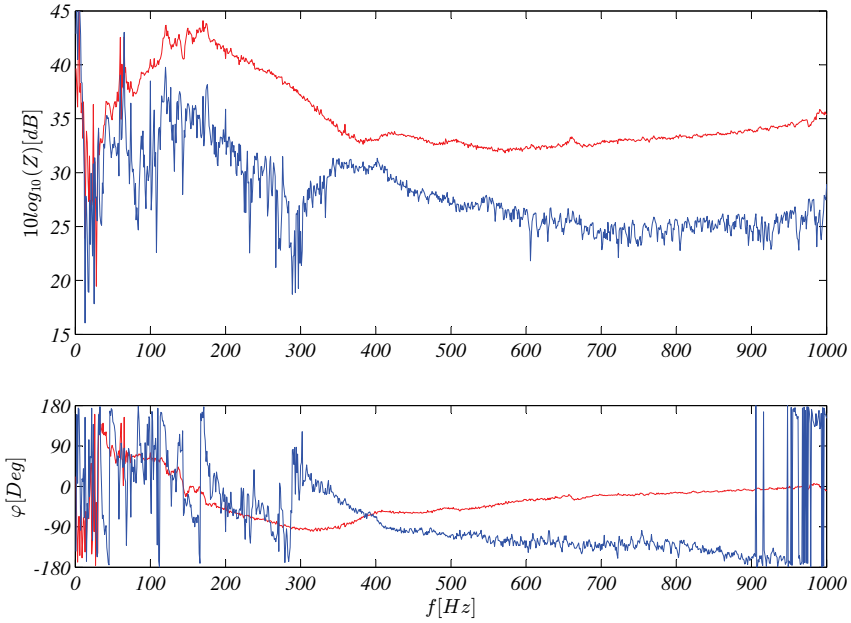

Figure 3.18: Bottom side surface input Z_{in}^{aa} (red) and transfer impedance Z_{tr}^{aa} (blue).

Mass- spring system 2

The top surface input and transfer impedance, Z_{in}^{bb} and Z_{tr}^{bb} respectively, are shown in Fig. 3.19. By observing the input impedance one can recognise the heavy layer (plus carpet) resonance on the foam layer at about $250Hz$, and the heavy layer resonance between the foam and the carpet at $550Hz$. The liner impedance is dominated by the mass of the heavy layer and the carpet in between the two resonances and by the stiffness of the foam below the first resonance. At high frequencies, above the heavy layer resonance between foam and carpet the impedance is dominated by the stiffness of the carpet. Below $150Hz$ the effect of mass radiation impedance of the vertical edges is visible. Some measurement inaccuracies can be recognised below $100Hz$. The anti-resonace peak $550Hz$ shows too little damping, an effect which is strongly influenced by the air gap correction which appears to become very critical at these frequencies. The top to bottom face cross and cross-transfer impedance, Z_{in}^{ba} and Z_{tr}^{ba} respectively, are shown in Fig. 3.20. The bottom to top face cross and cross-transfer impedance, Z_{in}^{ab} and Z_{tr}^{ab} respectively, are shown in Fig. 3.21. The comparison between the cross and cross-transfer terms of Fig. 3.20 and 3.21 shows that the cross and cross-transfer terms are approximately reciprocal. Furthermore, different boundary conditions and excitations mechanism are applied and the top and bottom face of the liner during the characterisation procedure. For $f > 600Hz$ the trends of the amplitude and of the phase

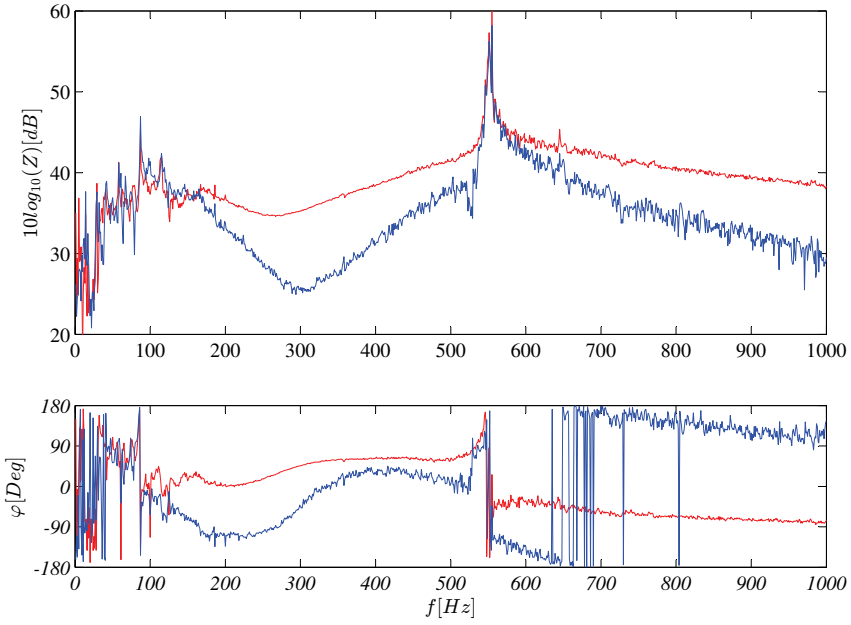

Figure 3.19: Top side surface input Z_{in}^{bb} (red) and transfer impedance Z_{tr}^{bb} (blue).

indicate the onset of the wave propagation across the thickness of the liner. Moreover, the term Z_{tr}^{ab} is characterised by slightly higher noise level compared to Z_{tr}^{ba}. The bottom surface input and transfer impedance, Z_{in}^{aa} and Z_{tr}^{aa} respectively, are shown in Fig. 3.22. Below $100Hz$ the effect of mass radiation impedance of the vertical edges is visible. At $350Hz$ the resonance between the mass of the heavy layer and carpet on top of the foam appears. For $f > 600Hz$ a constant amplitude and a $0deg$ phase indicates that the propagating wave is damped across the thickness of the liner and no energy is reflected back. Below $100Hz$ and at $300Hz - 400Hz$ some measurement errors can be recognised since the phase of the input impedance exceeds $\pm 90deg$. At frequencies below $100Hz$ the transfer and cross-transfer impedances are not reliable due to structural modes of the test rig and signal to noise problems.

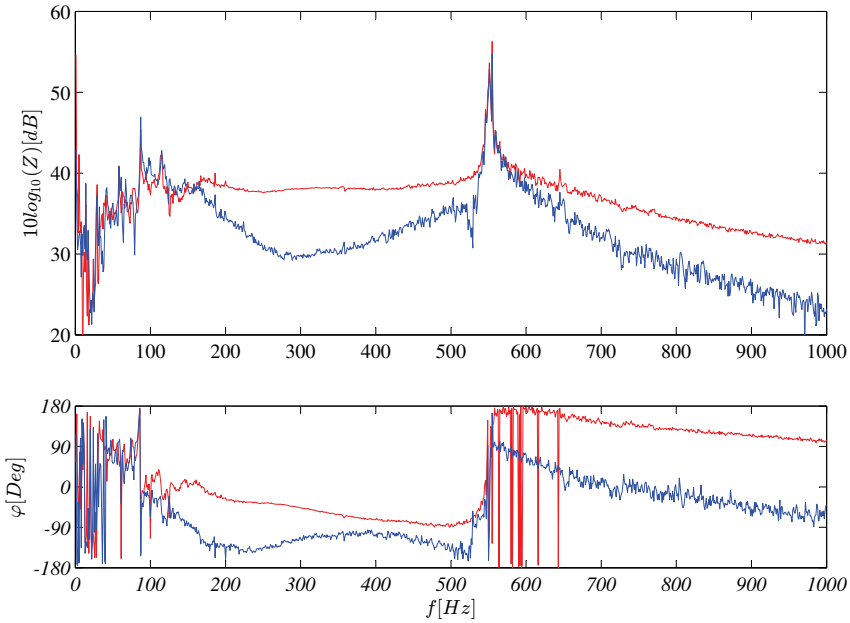

Figure 3.20: Top to bottom cross input Z_{in}^{ba} (red) and transfer impedance Z_{tr}^{ba} (blue).

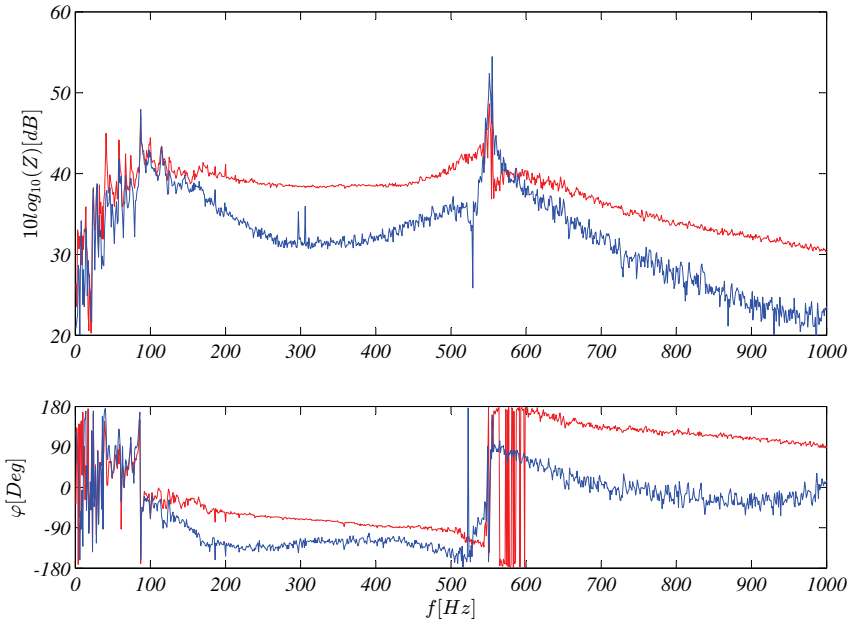

Figure 3.21: Bottom to top cross input Z_{in}^{ab} (red) and transfer impedance Z_{tr}^{ab} (blue).

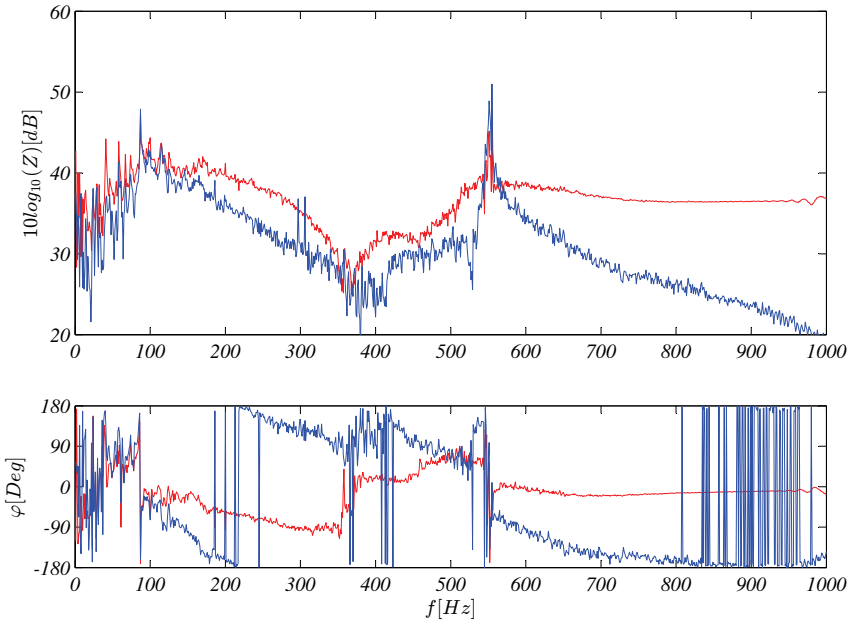

Figure 3.22: Bottom side surface input Z_{in}^{aa} (red) and transfer impedance Z_{tr}^{aa} (blue).

Chapter 4

Experimental validation

4.1 Sub-system characterisation

The proposed method has been validated by means of a test case. A clamped metal plate has been damped with a layer of porous material and coupled with a rigid rectangular cavity, see Fig. 4.1. The plate has dimensions of $1.7m$ times $0.8m$. Two different plate have been used in this work. A steel plate of $2mm$ thickness and an aluminium plate of $5mm$ thickness. Two sound packages have been used as a damping layer. First, a panel of Basotect TG melamine foam with the same dimension of the plate and a thickness of $42mm$. Second, a mass-spring system made of a $14mm$ PU foam attached to a rubber heavy layer of $3mm$ thickness. The acoustic fluid cavity is made by reinforced concrete rigid walls with inner dimension of $1.7m$ times $0.8m$ times $1m$. The single sub-systems have been characterised separately in an experimental, numerical or analytical manner, next the PTF method has been applied in order to assess the behaviour of the assembled system. The response obtained at a given position inside the acoustic cavity by means of PTF approach has been compared with a reference direct measurement of the assembled system.

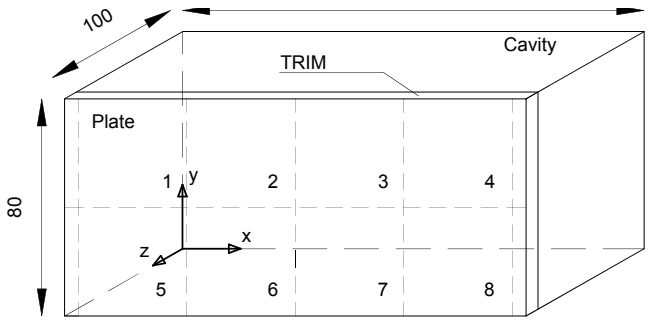

Figure 4.1: Discretisation of the interfaces and dimensions in cm of the test case.

4.1.1 Structure characterisation

To determine the mobility matrix Y of a structure we must, in principle, excite with a surface pressure at patch j and leave all the other patches free with $\overline{p}_{k\neq j} = 0$. Then the mobility relation between patch i and the patch j is given by the ratio of averaged surface velocity to the averaged surface pressure, see Eq. (1.6). In real life conditions, it is not trivial to excite a steel structure with a uniform surface pressure. In order to overcome this bottleneck a uniform pressure excitation has been approximated by a superposition of point forces applied in phase. If a sufficiently high number of excitation points is uniformly distributed over patch surface a good approximation of a uniform pressure distribution is obtained. In order to capture the averaged vibration field on the receiving patch the structural velocity has been measured in N positions spatially distributed in accordance with the Nyquist criterion taking into account the plate wavenumber. Thus the mobility relation between a patch j excited by means of N_j hammer blows and patch i is given by

$$Y_{ij} = \frac{\bar{v_i}}{\bar{p_j}} = \frac{1}{N_i N_j} \sum_{i=1}^{N_i} \sum_{j=1}^{N_j} \frac{v_{ikl}}{p_{jkl}} = \frac{1}{N_i N_j} \sum_{k=1}^{N_i} \sum_{l=1}^{N_j} Y_{ijkl}, \tag{4.1}$$

where $\bar{v_i}$ is the averaged structural velocity results of N_i measurement position in the receiving patch i and $\bar{p_j}$ is the approximated uniform imposed pressure as a results of N_j hammer blows on the excited patch j.

Steel plate

The steel plate used for the validation of the proposed methodology has been subdivided into 8 patches of dimensions $0.4m$ times $0.4m$. According to the Nyquist criterion this discretisation allows for a correct prediction of the sound radiation in the cavity up to $430Hz$. The patch mobility matrix of the plate has been measured by means of 16 accelerometers per patch and excited by means of 40 hammer blows per patch in accordance with Eq. 4.1. The density of the sensors allows capturing the plate vibration fields up to $500Hz$ without aliasing problems. The density of the excitation positions is sufficiently high to approximate a uniform pressure excitation for the given frequency range. The structural transfer function between the excitation position, where a point force has been applied by an impact hammer, and each patch has been measured by means of a Microflown pu-probe array.

Aluminium plate

The aluminium plate used for the validation of the proposed methodology has been subdivided into 32 patches of dimensions $0.2m$ times $0.2m$. According to the Nyquist sampling criterion this discretisation allows for a correct prediction of the sound radiation in the cavity up to $850Hz$. The patch mobility matrix of the plate has been measured by means of 9 accelerometers per patch and excited by means of 10 hammer blows per patch in accordance with Eq. (4.1). The density of the sensors allows capturing the plate

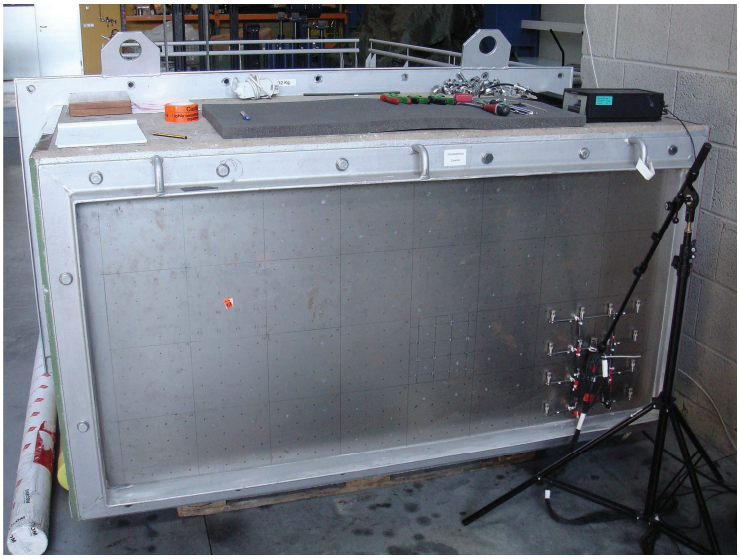

Figure 4.2: Characterisation of the structure: measurement of the structural transfer function vector between the excitation position (red spot) and the patches by means of a Microflown pu-probe array and an impact hammer.

vibration fields up to $1500Hz$ without aliasing problems. The density of the excitation positions is sufficiently high to approximate a uniform pressure excitation for the given frequency range.

4.1.2 Porous domain characterisation

Melamine

As shown in Fig. 3.3, the difference between the amplitude of the input and the transfer impedance is larger than $10dB$ starting from $200Hz$ in both experiment and numerical characterisation. Thus it is possible to consider the material as not globally reacting so that the contribution from the patches located far away from the excited patch can be neglected. In other words, since the material damping is considerably high, only the next neighbouring patch is important for the PTF reconstruction. As a consequence, the impedance matrix of the trim can be approximated by a banded matrix. Therefore, the characterisation of the specimen can be carried out on a small sample just as large as two patches. In order to perform the reconstruction we assumed that the cross impedance of the trim (through the thickness) is equal to the surface one. For the melamine foam, since the wavelength inside the interstitial fluid is much longer than the thickness of the foam and therefore wave propagation is only possible in the transverse direction, this hypothesis is acceptable in the investigated frequency range.

Mass-spring damping system

A mass-spring liner composed by a $14mm$ PU foam with $69kg/m^3$ density topped by a $3kg/m^2$ heavy layer has been used in the test case. This liner has been characterised by means of the trim test rig based on patch discretisation of $20cm$. Since foam and heavy layer are highly damped the energy decay is relatively fast compared to the distance between two neighbours patches. Thus it is possible to consider the material as quasi-locally reacting. Therefore only the next neighbours transfers terms are relevant for the PTF reconstruction. The impedance matrices of the material can be approximated by a banded matrix.

4.1.3 Fluid cavity characterisation

Since the fluid problem of the test case is a rectangular air cavity an analytical model superposition can be used, see [2], [7]. The patch transfer function between a patch and a point inside the fluid domain is given by:

$$Z^C(\boldsymbol{r}, \boldsymbol{r'}) = j\omega\rho_0 c_0^2 \frac{\phi_i(\boldsymbol{r})\phi_i(\boldsymbol{r'})}{\omega_i^2 - \omega^2 + 2j\epsilon\omega} sinc\left(\frac{m_{x,i}\pi\Delta x'}{Lx}\right) sinc\left(\frac{m_{x,i}\pi\Delta y'}{Ly}\right), \tag{4.2}$$

where r are the coordinates of the point and $r\prime$ are the coordinates of the centre point of the patch, $\delta x\prime$ and $\Delta y\prime$ are the dimensions of the patch. $\phi_i(r)$ and ω_i are the eigenmodes and the eigenfrequencies of the problem governed by the Helmholtz equation, respectively. The patch transfer function between two patches writes:

$$Z^C(\boldsymbol{r}, \boldsymbol{r'}) = j\omega\rho_0 c_0^2 \frac{\phi_i(\boldsymbol{r})\phi_i(\boldsymbol{r'})}{\omega_i^2 - \omega^2 + 2j\epsilon\omega} sinc\left(\frac{m_{x,i}\pi\Delta x}{Lx}\right) sinc\left(\frac{m_{x,i}\pi\Delta y}{Ly}\right) sinc\left(\frac{m_{x,i}\pi\Delta x'}{Lx}\right) sinc\left(\frac{m_{x,i}\pi\Delta y'}{Ly}\right), \tag{4.3}$$

where r and $r\prime$ are the coordinates of the centre point of the patches, Δx, Δy and $\Delta x\prime$, $\Delta y\prime$ are the dimensions of the patches. In order to account for the walls absorption and the losses in the fluid the equivalent damping coefficient ϵ of the cavity is introduced. Its value is determined by a modal updating procedure: the PTF reconstruction of the bare plate coupled to the acoustic cavity has been compared with the reference measurement of the assembled system in order to assess the right value of ϵ.

4.2 Assembled system

Two test case have been considered in this work. First, a steel plate coupled with the melamine liner and the air cavity and a patch discretisation of $40cm$. Second, an aluminium plate coupled to the mass-spring liner and the air cavity, and a patch

	x [m]	y [m]	z [m]
mic1	0.270	0.525	0.495
mic2	0.870	0.365	0.425
mic3	1.460	0.285	0.680

Table 4.1: Position of the receiver microphones inside the cavity for test case 1.

discretisation of $20cm$.

4.2.1 Case 1: steel plate and melamine foam

In the first step the clamped steel plate has been coupled directly to the cavity whereas in a second step the melamine liner has been applied on the steel plate and coupled with the rigid cavity. These two conditions allow us to check if the amount of damping taken into account by the PTF is representative of the real test case. The system has been excited in a point force located at (x = 0.35 m, y = 0.5 m, z = 1 m), by means of an impact hammer. The sound pressure level (SPL) has been measured in three positions inside the rigid cavity during the reference measurement. The coordinates of the microphone position are shown in Table 4.1, a picture of the interior of the acoustic cavity is shown in Fig. 4.3. The response of the microphones has been compared

Figure 4.3: Inner view if the acoustic cavity: the plate is partially coated by the melamine liner, the three receiver pressure microphones are visible.

with the PTF reconstruction. The steel plate has been characterised in an experimental fashion. The trim has been characterised in a numerically and in an experimentally way. The cavity has been modelled by an analytical solution. In order to solve the coupled

problem the solution of the system Eq. (1.20) has to be determined and finally, the SPL at the receiver position inside the cavity is given by Eq. (1.21). In case of a bare plate coupled to the rigid cavity Eqs.(1.12) and (1.13) are used instead.

In Fig. 4.4 is shown the comparison between two reference measurements conducted on the bare plate coupled to the cavity and on the coated plate coupled to the cavity. The melamine foam introduces damping in the system. It mainly influences the cavity absorption especially above 200 Hz since the thickness of the liner (42 mm) is too small to add absorption in the very low frequency range. Furthermore, the trim does not

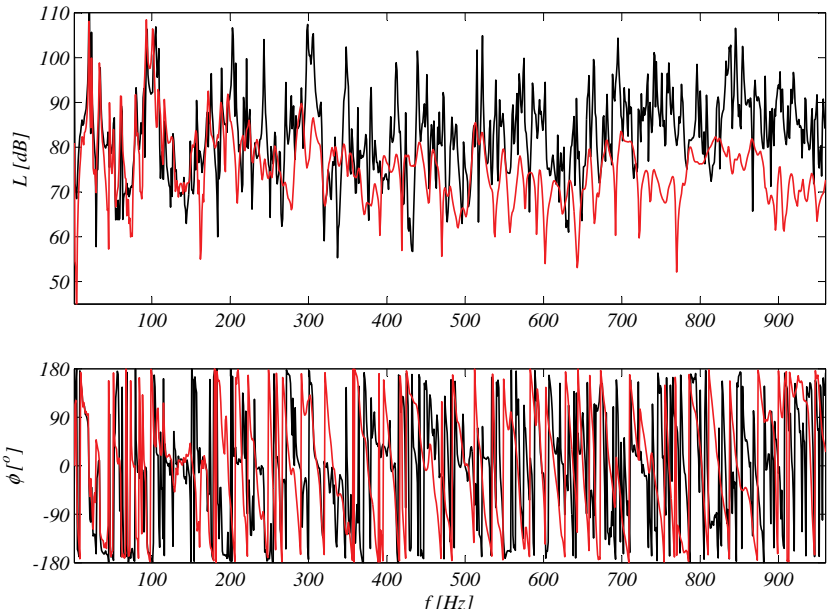

Figure 4.4: Comparison between the predicted SPL inside the cavity at position 1: reference measurement on the bare plate-cavity system (black) and on the trimmed plate-cavity system (red).

introduce structural damping on the plate. This is can be understood by comparing the patch mobilities of the subsystems, see Fig. 4.5. The input mobilities of the cavity are in the same order of magnitude of the trim mobility, while the structural mobilities of the plate are much lower. Only in a limited region below 100 Hz the plate mobility approach the trim mobility. Thus the main interaction occurs between the liner and the cavity. In addition, the main differences caused by varying the boundary conditions in the characterisation phase influence the liner impedance in the low frequency range, where the liner does not interact significantly with the cavity and the plate. Thus, the effects of the boundary conditions during the characterisation do not have an impact on the PTF reconstruction, for this trim variant.

The PTF reconstruction on the bare plate coupled with the cavity compared to the reference measurement is shown in Fig. 4.6. The purpose of this exercise is to perform a calibration of the cavity analytical model. As explained beforehand, through

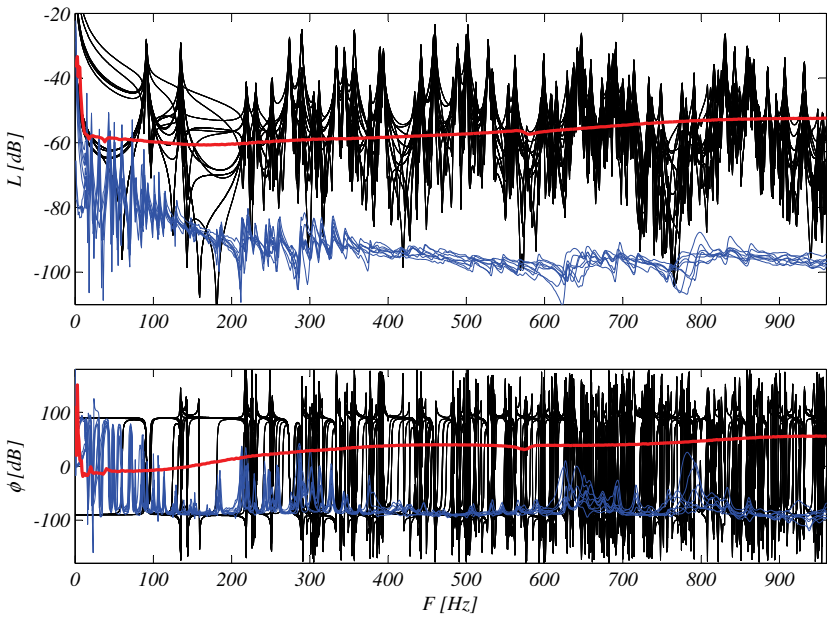

Figure 4.5: Comparison between the patch input mobility level of the bare plate (blue), trim (red) and cavity (black).

this reconstruction the value of the equivalent damping coefficient ϵ, accounting for the losses in the acoustic cavity, is determined by comparing the PTF reconstruction with the reference curve. The prediction of the SPL at position 1 is excellent up to 430 Hz, which is the theoretical limit for the given discretisation. Nevertheless the proposed method still yields reliable prediction even at higher frequencies, except for a narrow band between 430 Hz and 500 Hz and around 900 Hz.

In Fig. 4.7 the comparison between the reconstruction and the reference measurement is shown for the case where both plate and trim are characterized in an experimental manner. The method proposed yields an adequate prediction of the full-system behaviour up to the limit of the methodology. As expected the PTF is not able to predict the SPL at the receiver once the frequency is higher than 430 Hz. However the overall trend is still captured.

Fig. 4.8 shows the comparison between the reconstruction and the reference measurement for the case, where the plate is characterized in an experimental manner, whiles the trim is described in a numerical manner. The same conclusions from the previous reconstruction still apply. As already mentioned, the PTF approach is a hybrid method: each sub-system can be characterised in a standalone way by means of the more appropriate technique.

In order to verify that the trim is not globally reacting, the PTF reconstruction has

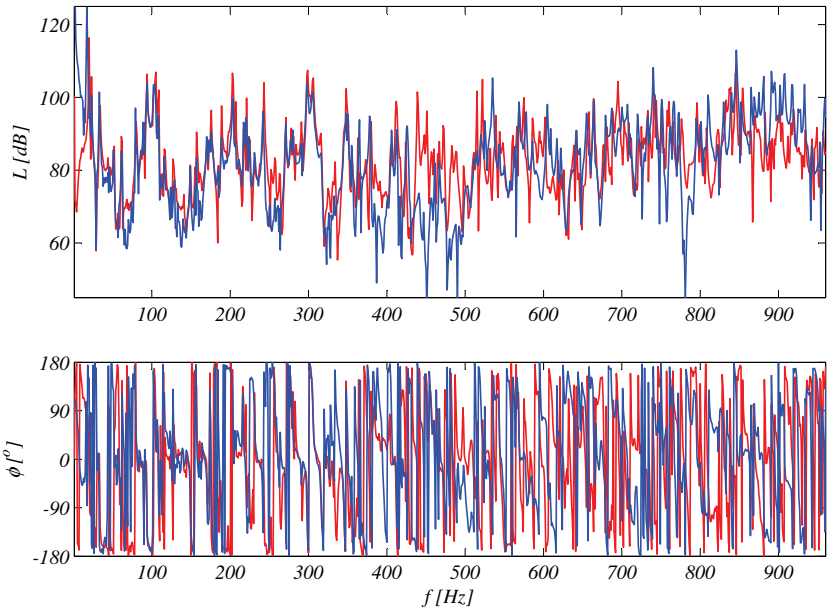

Figure 4.6: Comparison between the predicted SPL inside the cavity at position 1: PTF reconstruction (blue) and reference measurement (red). Experimental bare plate and analytical cavity.

been carried out with two different numerically characterised liners. The reconstruction has been performed first with a numerically characterised trim having the size of two patches, in order to mimic the experimental conditions. Next, the PTF has been applied with a numerically characterised liner having the size of the steel plate (8 patches) in order to take into account all transfer and cross (through the thickness) impedances. The result of this investigation is shown in Fig. 4.9. The two PTF reconstructions do match very well up to 500 Hz, small differences can be seen at higher frequencies, especially in the phase plot. In spite of these small discrepancies we can conclude that below the frequency limit imposed by the discretisation, it is not necessary to assess all the patch transfer function between the patches. Hence, the full trim impedance matrix can be reduced to a banded matrix where just the input and the next neighbour transfer surface impedances are accounted for. Moreover, this investigation has also proven that for the melamine foam the cross impedances can be approximated by the surface ones. As explained in [11] the required patch size for valid PTF results is governed by the fluid wavelength resulting in a rather coarse spatial discretisation scheme. This allows for efficient experimental characterisation. The patch averaging scheme for the structural mobility matrix, on the other hand, in principle requires a spatial sampling criterion which depends on the structural wavelength, but the utilisation of multiple

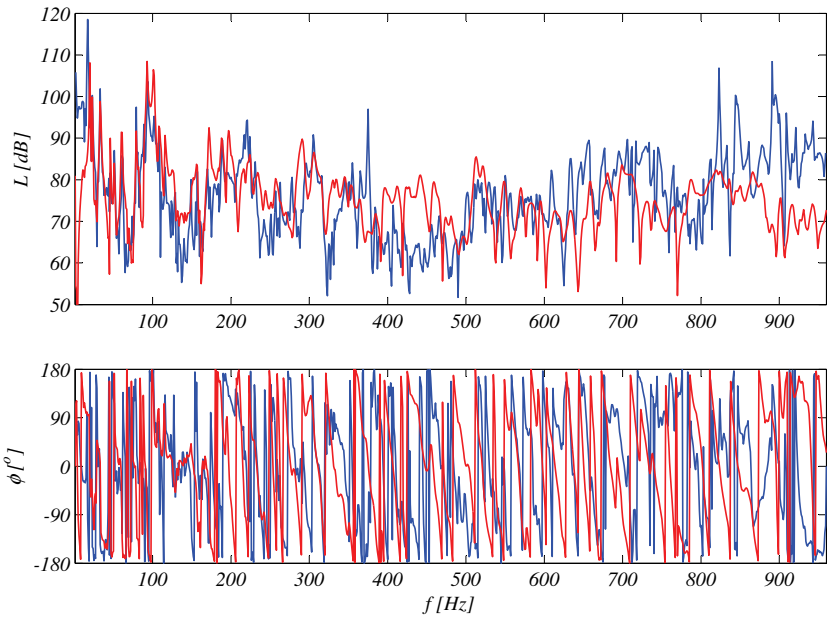

Figure 4.7: Comparison between the predicted SPL inside the cavity at position 1: PTF reconstruction (blue) and reference measurement (red). Experimental plate and experimental trim.

sensors on the receiving patch and random hammering on the excited patch reduces the measurement efforts to an acceptable level.

4.2.2 Case 2: aluminium plate and mass-spring system

The mass-spring liner has been applied on the aluminium plate and coupled with the rigid cavity. The system has been excited in a point force located in the centre of patch 13 at (x = 0.95 m, y = 0.45 m, z = 1 m), by means of an impact hammer. The sound pressure level (SPL) has been measured in three positions inside the rigid cavity during the reference measurement. The coordinates of the microphone position are shown in Table 4.2. The response of the microphones has been compared with the PTF reconstruction given by Eqs. (1.20) and (1.21). The aluminium plate has been characterised in an experimental fashion. The trim component has been characterised in an experimentally way. The cavity has been model by an analytical solution.

In Fig. 4.10 is shown the comparison between a direct measurement and the PTF reconstruction at microphone position 1. The proposed methodology yields a good SPL prediction of the behaviour of the coupled system up to $500Hz$. As expected the PTF diverges from the reference once the Nyquist sampling criterion is not fulfilled ($550Hz$ for the plate and $850Hz$ for the fluid). Up to $550Hz$ the patch discretisation is able to

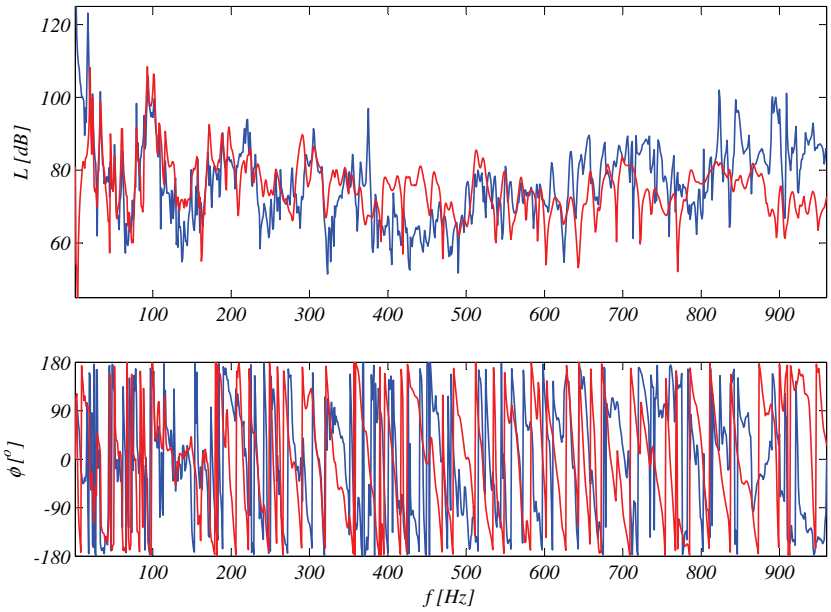

Figure 4.8: Comparison between the predicted SPL inside the cavity at position 1: PTF reconstruction (blue) and reference measurement (red). Experimental plate and numerical trim.

correctly approximate the mode shapes of the plate. For $550Hz < f < 850Hz$ only the acoustic field is correctly approximated by the patches. Spikes for $100Hz < f < 200Hz$ appear in the PTF reconstruction due to inaccuracies in the liner characterisation.

The PTF reconstruction of the bare system is compared to the reference measurement with trim in Fig. 4.11. This comparison allows to investigate the influence of the liner on the plate-cavity system. A reduction up to $10dB$ in the SPL is observed at and above the resonance region of the liner ($300Hz$). Below the resonance region the modes are slightly shifted because of the mass-loading effects of the liner on the plate. In Fig. 4.12 is shown the comparison between the PTF reconstruction at microphone position 1 assuming a locally reacting liner compared to the direct measurement. If the liner is assumed to be

	x [m]	y [m]	z [m]
mic1	0.775	0.660	0.335
mic2	0.225	0.190	0.365
mic3	1.445	0.330	0.490

Table 4.2: Position of the receiver microphones inside the cavity for test case 2.

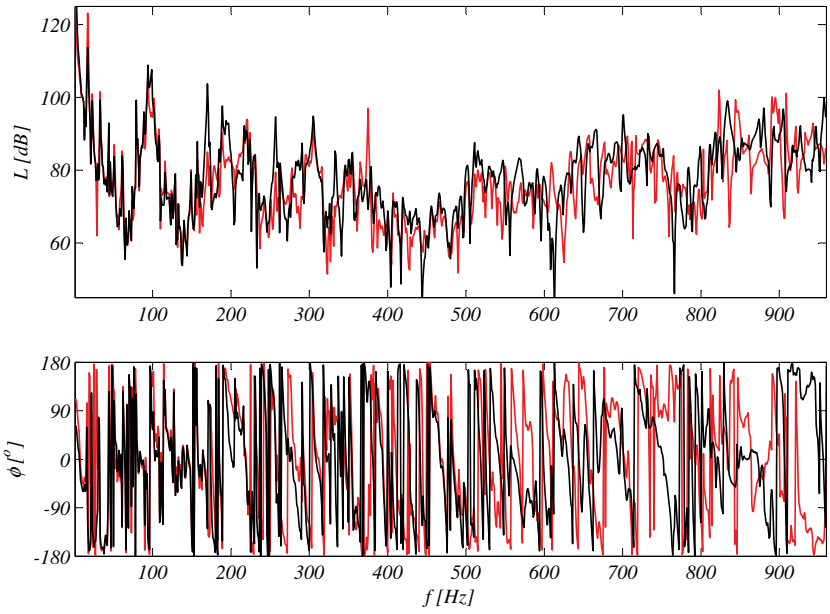

Figure 4.9: Comparison between the predicted SPL inside the cavity at position 1: PTF reconstruction where the trim is: numerically characterised (red) and numerically characterised by modelling a sample of same dimension as of the plate (black).

locally reacting, only the input term are accounted for in the PTF reconstruction. This assumption a strong influence in the low frequency range, for $f < 150Hz$, where the PTF prediction poorly approximate the reference line. However, at higher frequencies the quality of the reconstruction is not deteriorated compared to the one in Fig. 4.10. The liner can be considered as locally reacting only in the high frequency range, above the mass-spring resonance. Therefore, in order to assess a reliable prediction of the behaviour of the coupled system transfer terms must be taken into account.

4.3 Conclusions

Let us consider the test case 1, where the PTF has been applied to a $2mm$ thick steel plate with a patch size of $40cm$. According to Fig. 4.13 a sound power error of $-4dB$ is expected in the frequency range between the structural and the acoustic Nyquist frequency, $22Hz$ and $370Hz$ respectively. By applying the procedure presented in Paragraph 2.6 the frequency limit for a given error of $\pm 4dB$ results in $321Hz$. The trend presented in Fig. 2.10 can be recognised in terms of SPL in Fig. 4.14, where the PTF reconstruction of the bare plate-cavity system is compared to the reference measurement. An excellent match can be observed below $100Hz$. For $100Hz < f < 350Hz$ the

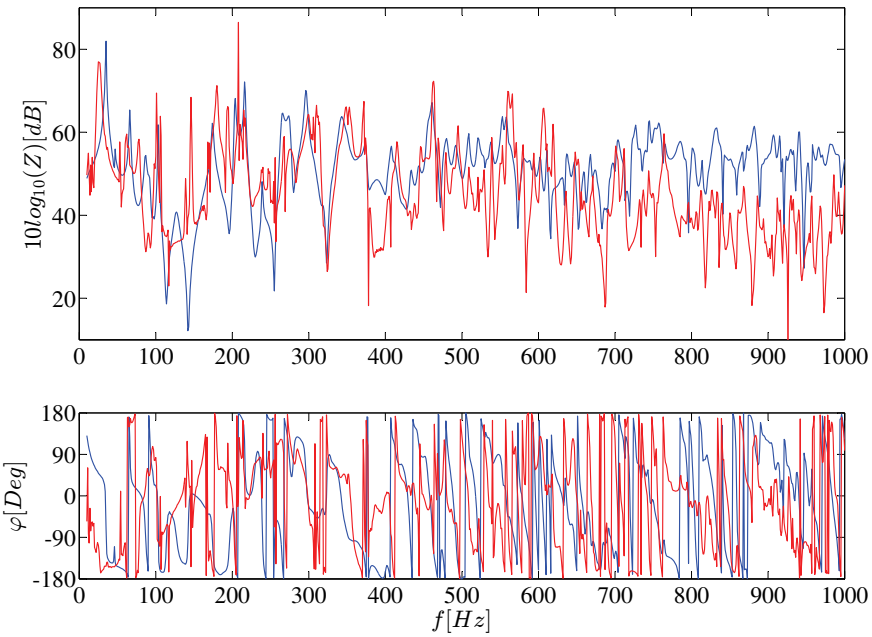

Figure 4.10: Comparison between the predicted SPL inside the cavity at position 1: PTF reconstruction (red) and reference measurement (blue).

PTF reconstruction underestimate the direct measurement at the resonances. Around $300 - 330Hz$ the PTF reconstruction recovers and at higher frequencies it diverges.

In the test case 2, where the aluminium plate is coupled to the rigid cavity and a patch size of $20cm$ is considered, an error of $\pm 0.5dB$ is expected for $f_{Ns} = 140Hz < f < f_{lim} = 530Hz$, see Fig. 4.13. From these examples it may be concluded that the presented procedure allows to significantly extend the frequency band of applicability of the PTF approach, depending on the desired accuracy in the calculation scheme. Although the sound power estimation is accurate in the valid frequency range, the sound field variables (local sound pressure and particle velocity) may show significantly deviations respect to the actual values. This is due to the fact that the patch-plate cannot reproduce the actual mode shapes of the plate realising different directivity patterns. Therefore the PTF prediction in terms of SPL in a single point may show different accuracy depending on the position of the receiver in the cavity. The presented sampling criterion is only valid for a structural-fluid coupled problem where the near field of the radiating surface is not dissipative. It is not valid for the case of a structure radiating into a dissipative media. In this case the choice of the patch dimensions must be based on the structural Nyquist sampling criterion.

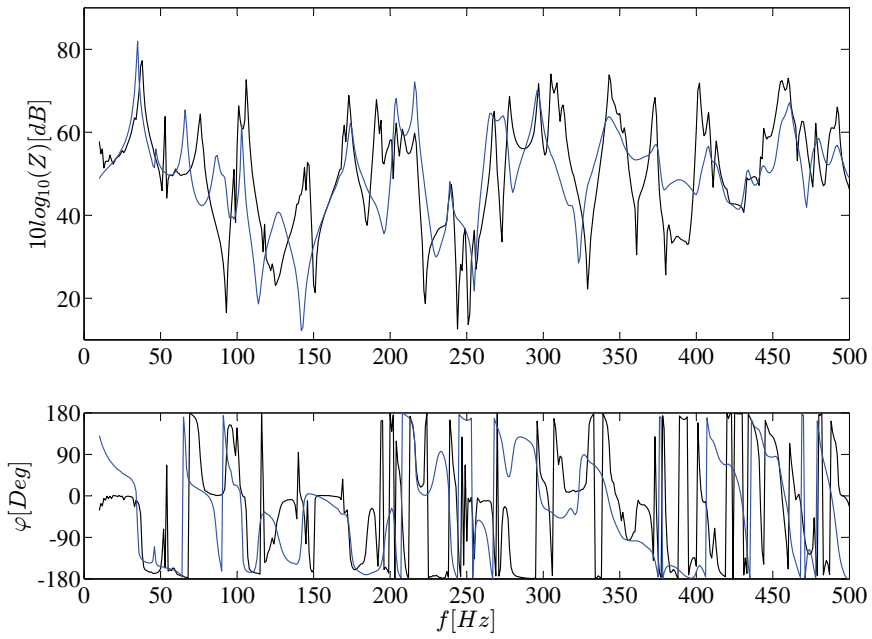

Figure 4.11: Comparison between the predicted SPL inside the cavity at position 1: PTF reconstruction without liner (black) and reference measurement (blue).

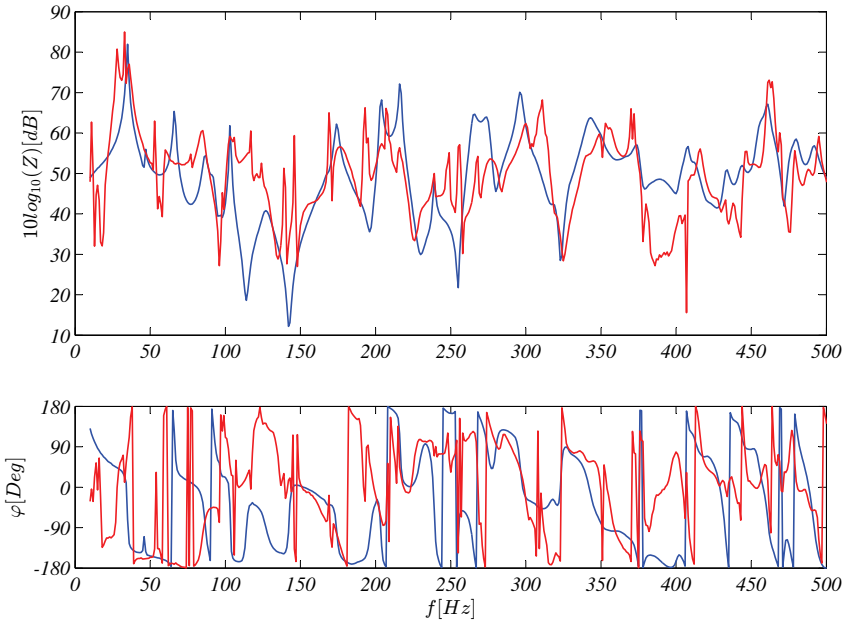

Figure 4.12: Comparison between the predicted SPL inside the cavity at position 1: PTF reconstruction with locally reacting liner (red) and reference measurement (blue).

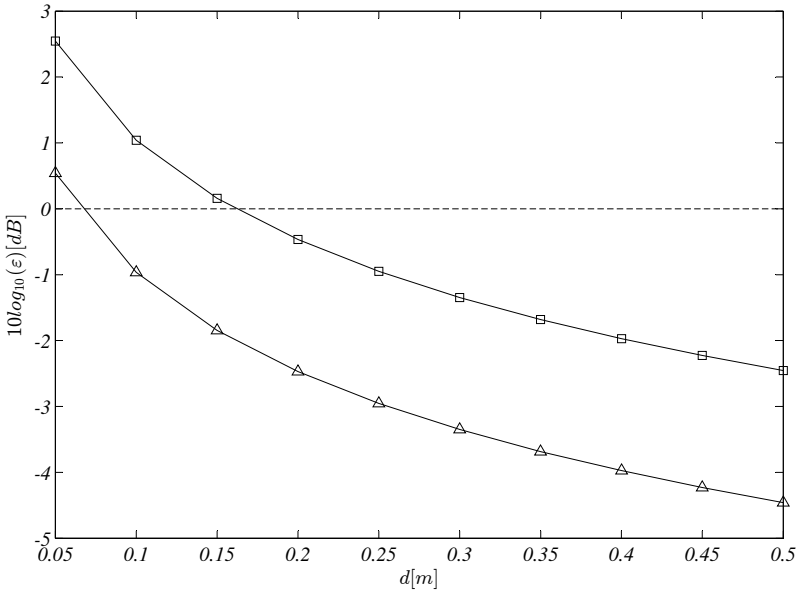

Figure 4.13: Error in the PTF sound power estimation as a function of the patch size d for a $2mm$ thick steel plate (triangle markers) and a $5mm$ thick aluminium plate (square markers).

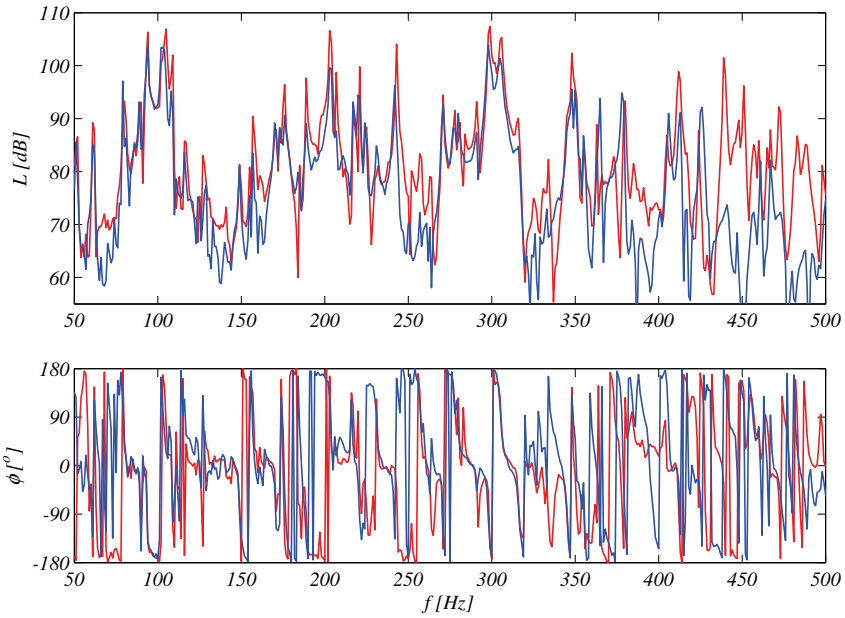

Figure 4.14: Comparison between the predicted SPL inside the cavity: PTF reconstruction (blue) and reference measurement (red) for a steel bare plate coupled with a rigid cavity. Patch size is $40cm$.

Conclusions

The PTF approach has been used to solve a coupled vibro-porous-acoustic problem. It allows for an independent characterisation of sub-systems and for coupling them at their interfaces via patch impedance matrices. The procedure is fully modular meaning its main advantage is that different procedures (numerical, experimental, analytical solution) can be used for the assessment of impedance relations of each sub-system. In this way, each sub-domain can be characterised by the most efficient technique allowing for a significant reduction of the measurement effort. Since the sub-systems are characterised in an independent manner, the PTF offers an efficient way to conduct variant studies. In this case, only the sub-systems which vary need to be re-characterised.

As a first achievement, a sampling criterion for the sound radiation of vibrating structures discretised into elemental areas has been investigated analytically. An accurate approximation of the radiated power may be obtained well beyond the frequency limit imposed by the structural Nyquist sampling criterion, provided the complex valued vibration field is averaged over each patch. By means of the presented theoretical study, it has been shown that, above the structural Nyquist frequency, the apparent reduction of the phase averaged velocity of the patch-plate is associated with an increased radiation efficiency in the valid frequency range. The two trends are equal and opposite, so that the acoustic power radiated by the patch-plate is equivalent to the one of the actual plate. If one allows for a well-defined error in the power estimation, acceptable in most of the acoustic applications, coarser patches can be chosen and consequently a substantial reduction of the experimental investigation time can be achieved. An analytical expression is given for the patch size as a function of the admissible error. The sampling criterion derived in this work has been applied and validated by means of numerical and experimental investigations. Although the sound power estimation is accurate in the valid frequency range, the sound field variables (local sound pressure and particle velocity) may show significant deviations with respect to their actual values. This is due to the fact that the patch-plate cannot reproduce the actual mode shapes of the plate realising different directivity patterns. The sampling criterion is exclusively valid for the radiation of a structure into a fluid, given a velocity field. It is not valid for radiation into dissipative media. In this case the plate near field becomes dissipative and the radiated power depends on the details of the velocity field.

As a next achievement, a novel experimental methodology for the assessment of the surface impedance of poroelastic lining materials has been presented and validated. The

method is fully compatible with the PTF approach, thus the information obtained can be seamlessly integrated into the PTF prediction of a coupled system. The main advantage consists in its time-efficiency and the possibility to consider the liner as a black-box, without the need for the characterisation of each layer's properties which might become highly involved. The measurement methodology described above is suited for multi-layered porous materials and it accounts for fluid-skeleton interaction. Nonetheless, the accuracy of the characterisation procedure is limited by sensor's signal to noise ratio and air gap correction. The data obtained from the test bench indicates that a reasonably accurate characterisation of multi-layered materials is possible in a frequency range of $100Hz - 1000Hz$.

Finally, the PTF approach has been applied to a plate-liner-cavity system and validated by means of a direct measurement on the coupled system. Two examples are given. First, a steel plate has been coupled to a melamine liner and a rigid acoustic cavity. In the latter example, an aluminium plate has been coupled to a liner with heavy layer and a rigid cavity. Furthermore, the untreated configuration (bare plate-cavity system) has been considered for both cases. The derived sampling criterion has been used in order to choose the patch dimensions based on a trade-off between the maximum valid frequency, precision in the power estimation and measurement effort. The impedance matrix of the plate has been assessed by means of experimental measurement while the cavity impedance matrix has been determined analytically. The liner impedance matrix has been assessed by means of the presented experimental methodology. In both test cases the PTF prediction provides a good agreement compared to the direct measurement, in the expected valid frequency range.

Acknowledgments

The research work of Giorgio Veronesi has been funded by the European Commission within the ITN Marie Curie Action project GRESIMO under the 7th Framework Programme (EC grant agreement no. 290050). The author would like to acknowledge the support of the "COMET K2 - Competence Centres for Excellent Technologies Programme" of the Austrian Federal Ministry for Transport, Innovation and Technology (bmvit), the Austrian Federal Ministry of Science, Research and Economy (bmwfw), the Austrian Research Promotion Agency (FFG), the Province of Styria and the Styrian Business Promotion Agency (SFG). Furthermore, the author express his gratitude to the consortium partners BMW AG, IAC GmbH, Microflown Technologies and Université de Sherbrooke for their support. Finally, the author gratefully acknowledges the support of COST action TU1105.

Bibliography

[1] M. Ouisse, L. Maxit, C. Cacciolati, J. Guyader, Patch transfer functions as a tool to couple linear acoustic problems, Journal of Vibration and Acoustics 127 (2005) 458,466. doi:10111512013302.

[2] G. Pavic, Air-borne sound source characterization by patch impedance coupling approach, Journal of Sound and Vibration (2010) 4907–4921.

[3] A. M. Maxit L., G. J., Improving the patch transfer function approach for fluid-structure modeling in heavy fluid, Journal of Vibration and Acoustics 134. doi:DOI:10.1115/1.4005838.

[4] C. D. Guyader J. L., Cacciolati C., Transmission loss prediction of double panels filled with porous materials and mechanical stiffners, Proceedings of ICA.

[5] J. Chazot, J. Guyader, Prediction of transmission loss of double panels with a patch-mobility method, Journal of the Acoustical Society of America 121 (2007) 267–278.

[6] T. N. Aucejo M., Maxit L., G. J., Convergence acceleration using the residual shape technique when solving structure-acoustic coupling with the patch transfer functions method, Computers & Structures 88(11-12) (2010) 728–736.

[7] J. Rejlek, G. Veronesi, C. Albert, E. Nijman, A. Bocquillet, A combined computational-experimental approach for modelling of coupled vibro-acoustic problems, SAE Technical Paper 2013-01-1997doi:10.4271/2013-01-1997.

[8] G. Veronesi, C. Albert, E. Nijman, J. Rejlek, A. Bocquillet, Patch transfer function approach for analysis of coupled vibro-acoustic problems involving porous materials, SAE Technical Paper 2014-01-2092doi:10.4271/2014-01-2092.

[9] C. Albert, G. Veronesi, E. Nijman, J. Rejlek, Patch impedance coupling of a structure-liner-fluid system based on direct experimental subsystem characterisation, submitted for review in Applied Acoustics.

[10] A. Leissa, Vibration of Plates, 1969.

[11] J. Allard, N. Atalla, Propagation of Sound in Porous Media, 2009.

[12] F. Fahy, P. Gardonio, Sound and Structural Vibration, Academic Press, 2007. doi:9780123736338.

[13] K. R. Holland, F. J. Fahy, An investigation into spatial sampling criteria for use in vibroacoustic reciprocity, ISVR Technical Report No 265.

[14] K. R. Holland, F. J. Fahy, A guide to the exploitation of vibroacoustic reciprocity in noise control technology, ISVR Technical Report No 264.

[15] G. Veronesi, E. Nijman, On the sampling criterion for structural radition into fluid, submitted for review in Journal of Sound and Vibration.

[16] M. Villot, C. Guigou, L. Gagliardini, Predicting the acoustical radiation of finite sixe multi-layered structures by applying spatial windowing ion infinte structures, Journal of Sound and Vibration 245(3) (2001) 433–455. doi:10.1006/jsvi.2001.3592.

[17] T. Vigran, Predicting the sound reduction index of finite size specimen by a simplified spatial windowing technique, Journal of Sound and Vibration 325 (2009) 507–512. doi:10.1016/j.jsv.2009.304.032.

[18] L. Cremer, M. Heckl, B. Petersson, Structure-Borne Sound: Structural Vibrations and Sound Radiation at Audio Frequencie, Springer, 2005. doi:978-3540226963.

[19] F. G. Leppington, E. G. Broadbent, F.R.S., K. H. Heron, The radiation efficiency of rectangular panels, Proceedings of the Royal Society of London A 382 (1982) 245–271.

[20] M. E. Delany, E. N. Bazley, Acoustical properties of fibrous absorbent materials, Applied Acoustics 3 (1970) 105–116. doi:10.1016/0003-682X(70)90031-9.